②

AL-TR-89-068   AD:

Final Report
for the period
September 1986 to
March 1989

Characterization of Tetrahydrogen via State–Selected Excitation of H_2

November 1989

Authors:
W.J. Marinelli
A.M. Woodward
W.J. Kessler

Physical Sciences, Inc.
Research Park
P.O. Box 3100
Andover MA 01810-7100

F04611-86-C-0077

Approved for Public Release

DTIC
ELECTE
DEC 27 1989
S **B** **D**

Prepared for the: **Air Force Astronautics Laboratory**

Air Force Space Technology Center
Space Division, Air Force Systems Command
Edwards Air Force Base,
California 93523-5000

89 12 26 139

NOTICE

FOREWORD

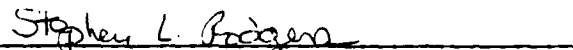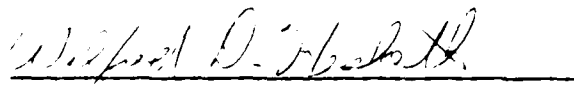This final report was submitted by Physical Sciences, Inc. on completion of Contract F04611-86-C-0077 for the Astronautics Laboratory (AFSC), Edwards AFB, CA. The Astronautics Laboratory Project Manager was Captain Steve Thompson.

This report has been reviewed and is approved for release and distribution in accordance with the distribution statement on the cover and on the DD Form 1473.

STEVEN D. THOMPSON, CAPT, USAF
Project Manager

STEPHEN L. RODGERS
Chief, ARIES Office

FOR THE DIRECTOR

WILFRED D. HESKETH
Acting Deputy Director
  Astronautical Sciences Division

REPORT DOCUMENTATION PAGE	Form Approved OMB No. 0704-0188

1a. REPORT SECURITY CLASSIFICATION Unclassified	1b. RESTRICTIVE MARKINGS

2a. SECURITY CLASSIFICATION AUTHORITY Unclassified	3. DISTRIBUTION / AVAILABILITY OF REPORT
2b. DECLASSIFICATION / DOWNGRADING SCHEDULE	Approved for public release. Distribution is unlimited.

4. PERFORMING ORGANIZATION REPORT NUMBER(S) PSI-1018/TR-924	5. MONITORING ORGANIZATION REPORT NUMBER(S) AL-TR-89-068

6a. NAME OF PERFORMING ORGANIZATION Physical Sciences, Inc.	6b. OFFICE SYMBOL (If applicable)	7a. NAME OF MONITORING ORGANIZATION Astronautics Laboratory

6c. ADDRESS (City, State, and ZIP Code) Research Park P.O. Box 3100 Andover MA 01810-7100	7b. ADDRESS (City, State, and ZIP Code) AL/LSX Edwards AFB CA 93523-5000

8a. NAME OF FUNDING / SPONSORING ORGANIZATION	8b. OFFICE SYMBOL (If applicable)	9. PROCUREMENT INSTRUMENT IDENTIFICATION NUMBER F04611-86-C-0077

| 8c. ADDRESS (City, State, and ZIP Code) | 10. SOURCE OF FUNDING NUMBERS |

PROGRAM ELEMENT NO.	PROJECT NO.	TASK NO.	WORK UNIT ACCESSION NO.
62302F	5730	00	VF

11. TITLE (Include Security Classification)

(U) Characterization of Tetrahydrogen via State-Selected Excitation of H_2

12. PERSONAL AUTHOR(S)
Marinelli, W.J., Woodward, A.M., and Kessler, W.J.

13a. TYPE OF REPORT Final	13b. TIME COVERED FROM 86/09/5 TO 89/03/5	14. DATE OF REPORT (Year, Month, Day) 89/11	15. PAGE COUNT 80

16. SUPPLEMENTARY NOTATION

17. COSATI CODES			18. SUBJECT TERMS (Continue on reverse if necessary and identify by block number)
FIELD	GROUP	SUB-GROUP	Tetrahydrogen, energy storage, high energy density matter, high spin nitrogen
21	09		
07	04		

19. ABSTRACT (Continue on reverse if necessary and identify by block number)

The initial effort to detect tetrahydrogen formed in a supersonic jet expansion was unsuccessful; the lifetime of tetrahydrogen was too short to permit detection. A study of the high-spin quintet nitrogen system was also conducted. Production of the A'- state was observed from energy pooling of triplet A- state molecules. Based on simple kinetic arguments, an upper limit of the lifetime of the A'- state was set at 0.3 ms.

20. DISTRIBUTION / AVAILABILITY OF ABSTRACT ☒ UNCLASSIFIED/UNLIMITED ☐ SAME AS RPT. ☐ DTIC USERS	21. ABSTRACT SECURITY CLASSIFICATION Unclassified
22a. NAME OF RESPONSIBLE INDIVIDUAL STEVEN D. THOMPSON, Capt, USAF	22b. TELEPHONE (Include Area Code) (805) 275-5651	22c. OFFICE SYMBOL AL/LSX

DD Form 1473, JUN 86   Previous editions are obsolete.

CONTENTS

iii

FIGURES

TABLES

1. PRODUCTION AND DETECTION OF H_4^*

1.1 $\underline{H}_4^*$ REVIEW

The four-center H_4 system has been the subject of theoretical studies since the late sixties, primarily due to interest in the relationship of the ground state hypersurface to the $H_2 + D_2 \rightarrow 2HD$ exchange reaction.[1,2,3] Investigations into the nature of the excited state(s) of such system have been limited in number even though SCF-MO-CI calculations in 1976 by Goddard and Csizmadia indicated the existence of a bound "excimer state".[4] Recently, however, Nicolaides et al., using an extension of their modeling work on rare gas hydrides[5] have predicted the existence of a bound singlet excited state of H_4 and have extended this analogy to the $(H_2)_3$ and $(H_2)_5$ clusters.[6,7]

The theoretical studies of Refs. 6 and 7 predict that the bound state of H_4 arises from reaction of molecular hydrogen in its ground state with H_2 that has been excited to the $B(^1\Sigma_u^+)$ state.

$$H_2(B^1\Sigma_u^+) + H_2(X^1\Sigma_g^+) + M \rightarrow H_4^* + M \quad . \tag{1}$$
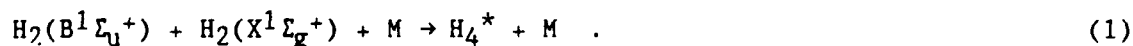
Further, the stable excited state is predicted to be produced only when the $B^1\Sigma_u^+$ state precursor has sufficient "ionic" character for reaction with $H_2(X)$. This is predicted to occur for $v \geq 3$ in the upper state.[6,7]

Quenching studies of $HD(B,v)$ performed by Atkins, Moore, and coworkers[8-10] show an unusually large quenching cross section (79Å^2) for H_2. This had led to further speculation that formation of a complex is involved. The $H_2(B)$ state in $v' = 3$ has sufficient energy to dissociate itself as well as an H_2 collision partner:

$$H_2(B) + H_2 \rightarrow 4H \qquad \Delta E = -2.70 \text{ eV} \quad .$$

Hence, quenching of $H_2(B)$ by H_2 may be highly reactive with H-atoms as the products.

The calculations of Nicolaides and coworkers[5-7] show that H_4^* is bound by 3.1 eV with respect to dissociation to form $H_2(B)$ and H_2. However, they also have shown that the complex is bound by 1.86 eV with respect to dissociation along the $H^- + H_3^+$ coordinate. Hence, photolysis of H_4^* may produce $H_3^+ + H^-$, $H_3 + H$, or $H_2(B) + H_2$. A careful selection of photolysis wavelengths may result in selective excitation into any of these channels. In our experimental effort we will be using a range of photolysis wavelengths in order to excite the channel leading to $H_2(B) + H_2$.

Little has been published concerning the structure and bond frequencies of the H_4^* excimer. The structure is predicted to be trigonal pyramidal, comprising a H_3^+ complex in an equilateral trigonal geometry of sides 0.899Å and and H^- center above the H_3^+ triangle at a bond distance of 2.01Å. The electron density of the structure is higher in the center than along the bonds.[6] Though bond vibrational frequencies for H_4^* have not been calculated, the structure of the H_3^+ center is quite similar to that calculated for free H_3^+. The calculations of Carney and Porter[11] have shown symmetric stretch and bending vibrational frequencies for the ion to be 3185 and 2516 cm^{-1}. Hence, in both laser photodissociation and passive emission studies of H_4^* progressions in these frequencies may be observed. Passive emission from the $H_4^*(^1A')$ origin may appear as progressions in the $H_2(X,v)$ system at frequencies shifted by the 3.1 eV binding energy of H_4^* with respect to the $H_2(B-X)$ Lyman system. Thus a careful study of both the absorption and emission spectrum of the excited mixture is required to detect H4* formed from the reaction of $H_2(B)$ with H_2.

1.2 DESIGN OF EXPERIMENTAL APPARATUS

The goal of the design phase of the experimental program was to produce a device which would enable us to produce $H_2(B,v')$ in a supersonic jet, provide a sufficient number of collisions with H_2 to produce H_4^*, and probe for its

existence and molecular properties. We chose to produce $H_2(B,v)$ in the jet by energy transfer from Ar^* resonance states (1048Å, 1066Å lines) in Ar/H_2 mixtures via discharge production of Ar^* in the nozzle expansion region.

Detection of H_4^* may be via observation of passive emission from the radiating excimer or via photodissociation of H_4^* to produce $H_2(B)$, which may be observed in emission.

1.2.1 <u>Nozzle Source</u>

The primary reason for using a supersonic molecular beam to produce H_4^* is to provide a locally high density but optically thin source of H_2 for direct excitation of the $H_2(B)$ state as well as collisional production and stabilization of H_4^*. Three primary criteria must be met by the source:

1. There must be sufficient collisions in the expansion beyond the nozzle throat for collisional quenching of $H_2(B)$ to occur at a rate at least comparable to that for spontaneous radiation.

2. When energy transfer from $Ar*$ to H_2 is employed there must be sufficient collisions beyond the nozzle threat for Ar^* to be quenched by H_2.

3. Formation of stabilized H_4^* is a three-body process. Hence, sufficient collisions must occur in the post-excitation region between the colliding $H_2(B)$ - H_2 complex and a third body (H_2 or Ar).

A further practical constraint is that the total gas flux from the system must be handled by a 2000 ls^{-1} diffusion pump. This was primarily a cost constraint.

These constraints are met using pulsed valves of the types reviewed by Gentry.[12] These valves typically have gas pulse durations of 100 to 500 μs at repetition rates up to 35 Hz. These duty factors are ideally suited to experiments employing pulsed lasers. Due to the reduced gas load realized by using these sources, smaller pumping systems may be employed to achieve desired background

pressures. Typically, the desired background pressure is set such that the molecular mean free path is comparable to dimensions of the background chamber. In our case this is approximately 10^{-4} Torr.

Gas flow in freely expanding supersonic jets has been treated extensively by Anderson and Fenn[13] and Fenn.[14] These sources are characterized by a rapid drop in number density, a decrease in kinetic temperature, and an increase in beam translational energy downstream of the nozzle throat. These properties are typically expressed in terms of the Mach number of the flow, M, and the distance downstream of the nozzle throat in nozzle diameters, (L/D). The number density, N, the temperature, T, and the velocity, V, are given by:

$$\frac{N}{N_0} = \left[1 + (\gamma - 1) M^2/2 \right]^{1/(1-\gamma)} \tag{2}$$

$$\frac{T}{T_0} = \left[1 + (\gamma - 1) M^2/2 \right]^{-1} \tag{3}$$

$$V = \left(\frac{\gamma KT}{m} \right)^{1/2} M \tag{4}$$

where γ is the heat capacity ratio of the gas (C_p/C_v) and the subscript zero denotes the nozzle plenum or "stagnation" conditions. The value of M must be determined numerically and has been tabulated by Anderson[15] as a function of (L/D) for various values of γ. The rapid drop in number density and temperature in these expansions is illustrated in Fig. 1.

We will use expressions (2) to (4) to define the nozzle operating conditions subject to the collisional quenching constraints imposed by our optical pumping methods. There is some question concerning the degree to which rotational degrees of freedom couple to translation in H_2. We have assumed they couple well in our calculations ($\gamma = 7/5$) as opposed to $\gamma = 5/3$. In the case of Ar^* quenching by H_2 to form $H_2(B)$ a quenching rate coefficient of $(1.9 \pm 0.5) \times 10^{-10}$ cm^3 molecule^{-1} s^{-1} has been measured by Boxall, Chapman, and Wayne.[16]

4
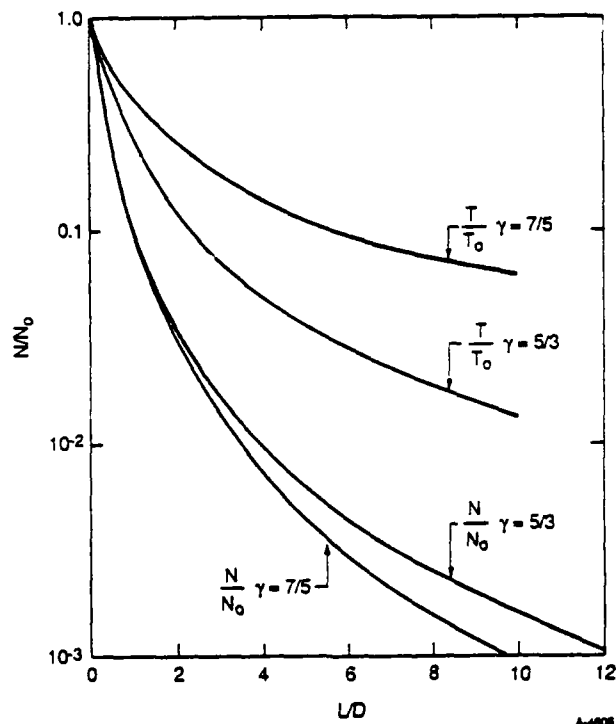
Figure 1. Supersonic nozzle reduced number density and temperature profiles for monatomic ($\gamma = 5/3$) and diatomic ($\gamma = 7/5$) gases.

The radiative rates for the Ar^* resonance lines are given by Wiese et al.[17] as $5.1 \times 10^8 s^{-1}$ (1048Å) and $1.19 \times 10^8 s^{-1}$ (1066Å). The condition for efficient quenching is

$$k_Q[H_2] \geq k_{rad}^{Ar^*} \quad . \tag{5}$$

If the faster radiative rate is employed, then we require $[H_2] \geq 2.7 \times 10^{18}$ molecules cm^{-3} for efficient quenching or Ar^*. For $H_2(B)$ quenching by H_2 the results of Fink, Atkins, and Moore[8] give a super-gas-kinetic quenching rate coefficient of 1.1×10^{-9} cm^3 molecule^{-1} s^{-1} at 300 K. The radiative rate for the B-state has been measured by Hessler[18] to be $1.25 \times 10^9 s^{-1}$. Hence H_2 concentrations in excess of 1.1×10^{18} molecules cm^{-3} are required to quench $H_2(B)$. Thus, at H_2 densities sufficient to quench Ar^* radiation $H_2(B)$ will also

5

be quenched. If the radiative rate for the Ar^* 1066Å line is used in expression (5) the H_2 quenching density obtained is 6.3 10^{17} molecule cm^{-3}. A useful practical H_2 quenching density is thus approximately 1 x 10^{18} molecule cm^{-3}.

Average mass flow through the nozzle is a function of the nozzle stagnation pressure, cross sectional area, flow velocity at the throat, and valve duty cycle. The pumping speed required to achieve a given background pressure is simply written as

$$\kappa_p = \frac{\pi}{4} f \tau_p D^2 V_0 N_0/N_B \qquad (6)$$

where f is the valve pulsing frequency ($10s^{-1}$), τ_p is the pulse duration ($10^{-4}s$), D is the nozzle throat diameter (cm), V_0 is the beam velocity at the throat (M = 1, V = 1.2 x 105 cm s^{-1}), N_0 is the stagnation number density, and N_B is the desired background number density (10^{-4} Torr = 3.3 x 10^{12} molecule cm^{-3}). The values of these parameters, where provided, are typical for the nozzle source under consideration. Figure 2 shows the pumping speed required to achieve 10^{-4} Torr operating pressure for four stagnation pressures (1, 2, 5, and 10 atm) as a function of nozzle throat diameter. The horizontal line on the plot defines the pumping speed of the Varian VHS-6 diffusion pump system appropriate to our system. The intersection of the diffusion pump line with the pumping speed curves define the appropriate operating nozzle diameters for each pressure. Using these values of N_0 and D we can use the curve in Fig. 1 to determine the distance from the nozzle throat at which the [H_2] is sufficient to quench both $H_2(B)$ and Ar^*. This is plotted in Fig. 3 and shows that the distance is approximately 0.9 mm and is independent of the combinations of N_0 and D which require the maximum pumping speed. Thus 0.9 mm is the maximum distance from the nozzle throat at which $H_2(B)$ can be excited and efficiently quenched.

We have chosen to employ a 5 atm nozzle stagnation pressure with a 250 μm diameter throat to continue the design calculations since, in our previous experience, this combination has been shown to be optimum for mechanical performance of the nozzle under consideration. The H_2 expansion centerline

6
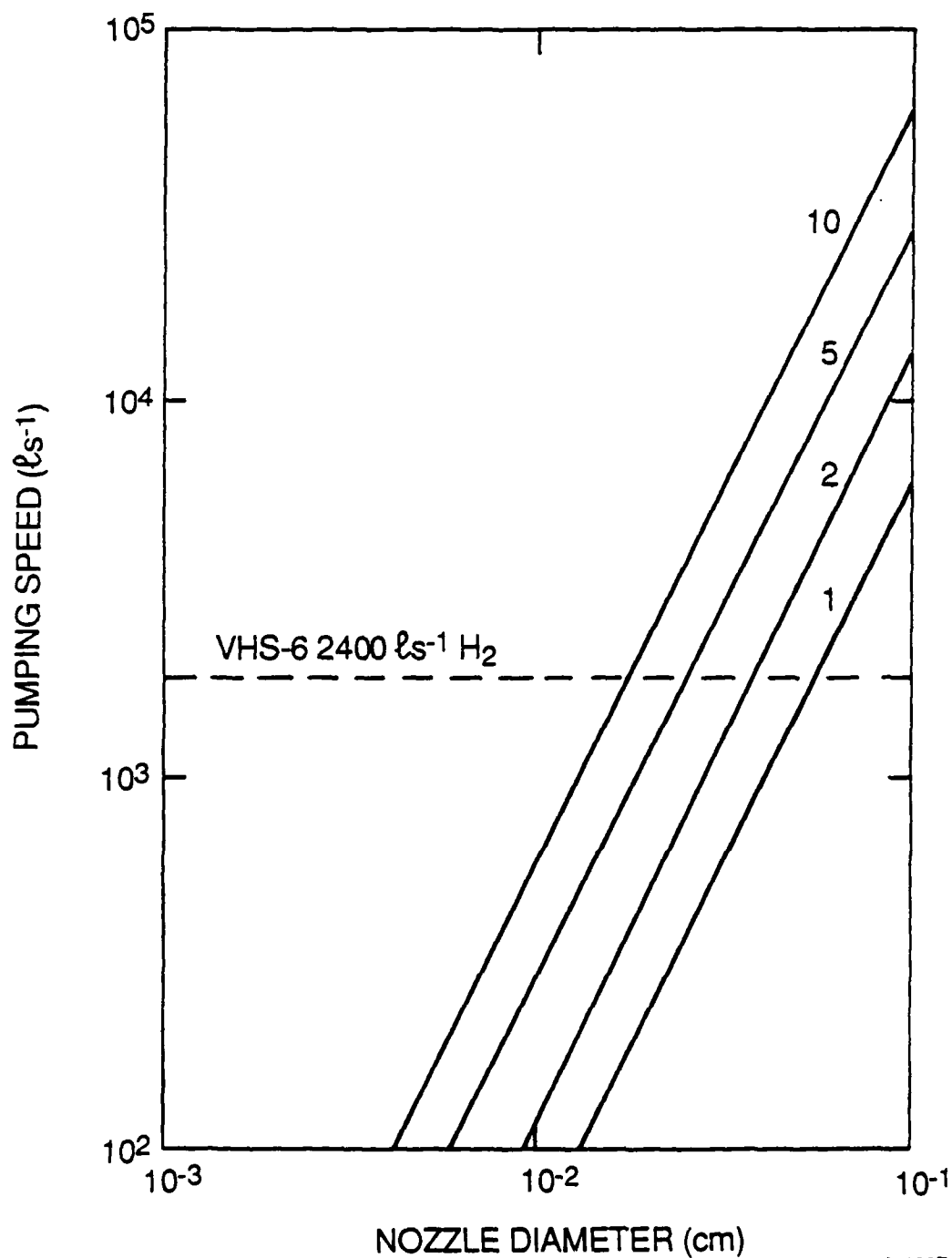
Figure 2. Average pumping speed required to maintain 10^{-4} Torr pressure as a function of nozzle throat diameter for H_2 stagnation pressures of 1, 2, 5, and 10 atmospheres.

7
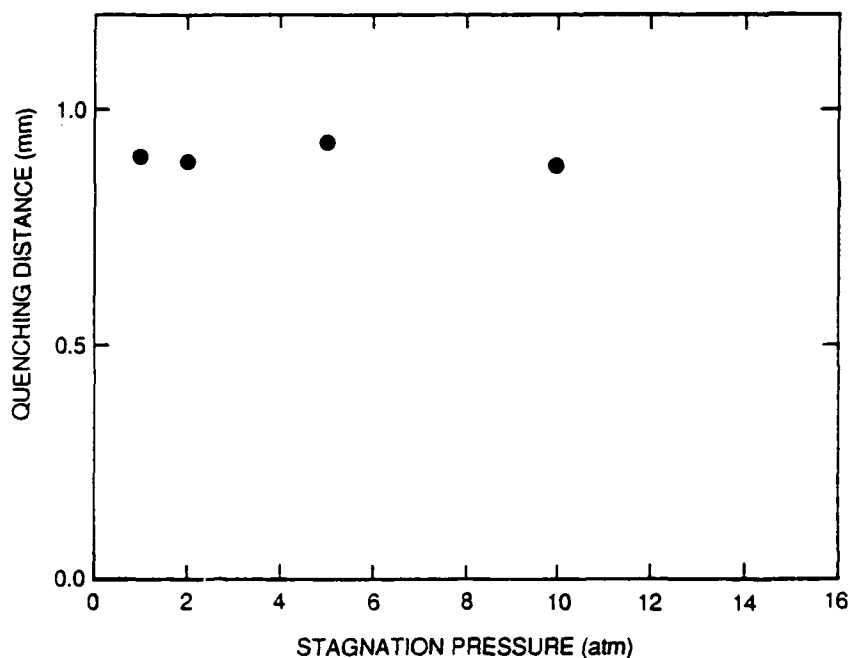
Figure 3. $H_2(B)$ quenching distance as a function of nozzle stagnation pressure.

number densities, kinetic temperature, and beam velocities are shown for these conditions as a function of distance from the nozzle throat in Figs. 4 to 6. The $H_2(B)$ and H_4^* collision rates may be calculated and integrated from these plots. The molecular collision rate is simply given from kinetic theory as:

$$Z = \sqrt{2}\ \pi\ \sigma\ \bar{c}\ N \tag{7}$$

where σ is the collision cross section and $\bar{c}$ is the average molecular velocity.

$$\bar{c} = \left(\frac{8\kappa T}{\pi m}\right)^{1/2} . \tag{8}$$

Hence, the collision frequency is a function of number density and pressure, both of which are decreasing with distance from the nozzle throat. The total number of collisions a molecule undergoes is simply the time integral of the collision frequency, which is decreasing with distance from the throat. In

8
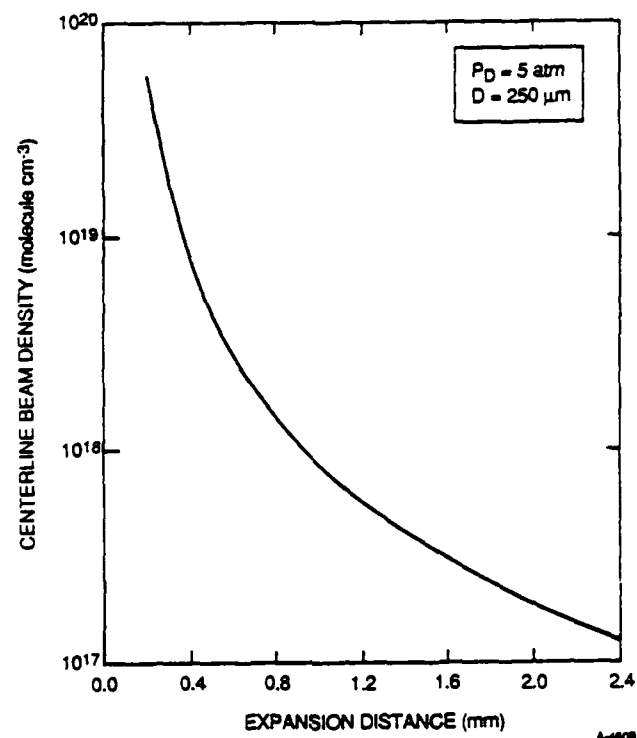
Figure 4. $H_2(B)$ nozzle expansion, H_2 centerline number density.
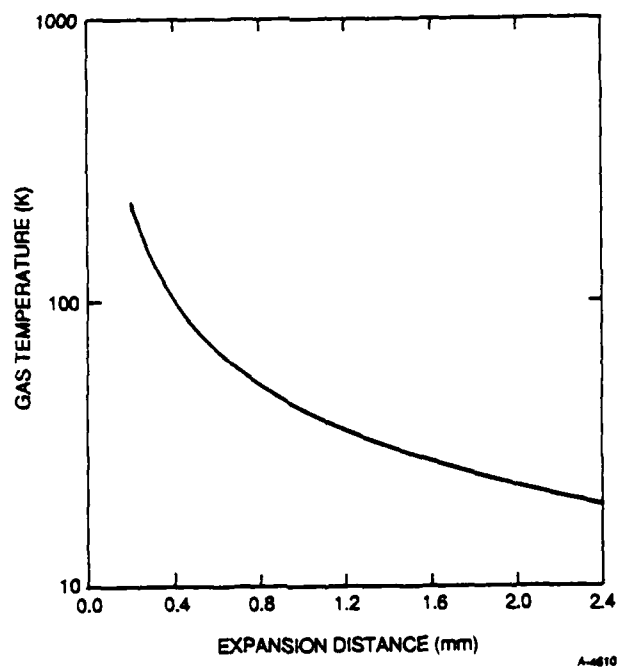
Figure 5. $H_2(B)$ nozzle expansion kinetic temperature.

9
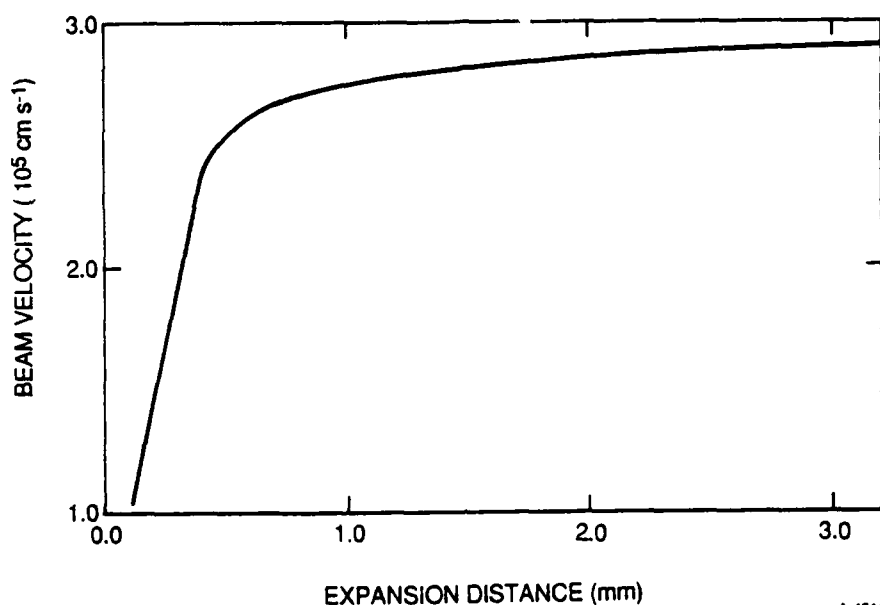
Figure 6. $H_2(B)$ nozzle expansion beam velocity.

divided by the beam velocity, which is also changing with distance. This integration and the other nozzle operating parameters are shown in Table 1. The integration shows that the H_4^* complex may undergo 300 collisions if formed 0.9 mm from the nozzle throat. This assumes a relaxation cross section identical to the $H_2(B)$ relaxation by $H_2(79\text{Å}^2)$. Stabilization of the H_4^* is essentially a two step process. This first step is the collisional stabilization of the orbiting $H_2(B)$ - H_2 complex during its lifetime. The second step involves quenching of the highly excited H_4^* to lower vibrational levels of the complex. The first step is the most critical because it requires that a collision occur in the 10^{-10} to 10^{-12}s during which the excited complex exists. This requires very high collision rates. Our estimate is that H_4 formation efficiencies in the range of 10^{-2} to 10^{-4} per $H_2(B)$ molecule excited may be expected. This would result in approximately 5×10^6 to 5×10^4 H_4 molecules being produced for each laser pulse. Detection sensitivities are difficult to estimate due to lack of any information about the H_4^* photodissociation cross section. If this cross section is in the range from 10^{-18} to 10^{-20} cm^2 then only modest

10

TABLE 1. Nozzle performance characteristics.

Total collisions = 306; L > 0.9 mm.

L/D	MACH NO.	T/T(0)	T	L(mm)	N/N(0)	N	V(cm/s)	LOG(N)	Z(1/S)	Z*t
0.4	0.00	1.00E+00	300.0	0.1	1.00E+00	1.2E+20	1.05E+05	20.08990	3.83E+11	
0.8	1.34	7.35E-01	220.4	0.2	4.62E-01	5.7E+19	1.52E+05	19.75501	1.52E+11	20818
1.2	2.44	4.57E-01	137.0	0.3	1.41E-01	1.7E+19	2.18E+05	19.23863	3.65E+10	5094
1.6	3.16	3.33E-01	100.0	0.4	6.42E-02	7.9E+18	2.41E+05	18.89725	1.42E+10	1105
2	3.72	2.65E-01	79.5	0.5	3.62E-02	4.4E+18	2.53E+05	18.64807	7.14E+09	432
2.4	4.19	2.21E-01	66.4	0.6	2.31E-02	2.8E+18	2.61E+05	18.45286	4.16E+09	220
2.8	4.60	1.91E-01	57.3	0.7	1.60E-02	2.0E+18	2.66E+05	18.29269	2.67E+09	130
3.2	4.97	1.69E-01	50.6	0.8	1.17E-02	1.4E+18	2.69E+05	18.15702	1.84E+09	84
3.6	5.30	1.51E-01	45.4	0.9	8.90E-03	1.1E+18	2.72E+05	18.03941	1.33E+09	58
4	5.60	1.38E-01	41.3	1	7.01E-03	8.6E+17	2.74E+05	17.93566	9.97E+08	43
4.4	5.88	1.26E-01	37.9	1.1	5.66E-03	7.0E+17	2.76E+05	17.84285	7.71E+08	32
4.8	6.15	1.17E-01	35.1	1.2	4.67E-03	5.7E+17	2.78E+05	17.75892	6.12E+08	25
5.2	6.40	1.09E-01	32.7	1.3	3.91E-03	4.8E+17	2.79E+05	17.68232	4.95E+08	20
5.6	6.63	1.02E-01	30.6	1.4	3.33E-03	4.1E+17	2.80E+05	17.61187	4.07E+08	16
6	6.86	9.61E-02	28.8	1.5	2.86E-03	3.5E+17	2.81E+05	17.54667	3.40E+08	13
6.4	7.07	9.09E-02	27.3	1.6	2.49E-03	3.1E+17	2.82E+05	17.48600	2.88E+08	11
6.8	7.28	8.62E-02	25.9	1.7	2.18E-03	2.7E+17	2.82E+05	17.42926	2.46E+08	9
7.2	7.48	8.21E-02	24.6	1.8	1.93E-03	2.4E+17	2.83E+05	17.37598	2.12E+08	9
7.6	7.67	7.84E-02	23.5	1.9	1.72E-03	2.1E+17	2.84E+05	17.32576	1.85E+08	7
8	7.85	7.50E-02	22.5	2	1.54E-03	1.9E+17	2.84E+05	17.27828	1.62E+08	6
8.4	8.03	7.20E-02	21.6	2.1	1.39E-03	1.7E+17	2.85E+05	17.23324	1.43E+08	5
8.8	8.20	6.92E-02	20.8	2.2	1.26E-03	1.6E+17	2.85E+05	17.19041	1.27E+08	5
9.2	8.37	6.67E-02	20.0	2.3	1.15E-03	1.4E+17	2.85E+05	17.14959	1.14E+08	4
9.6	8.53	6.43E-02	19.3	2.4	1.05E-03	1.3E+17	2.86E+05	17.11059	1.02E+08	4
10	8.69	6.21E-02	18.6	2.5	9.62E-04	1.2E+17	2.86E+05	17.07326	9.20E+07	3
10.4	8.84	6.01E-02	18.0	2.6	8.86E-04	1.1E+17	2.86E+05	17.03746	8.33E+07	3
10.8	8.99	5.82E-02	17.5	2.7	8.19E-04	1.0E+17	2.87E+05	17.00308	7.58E+07	3
11.2	9.14	5.65E-02	16.9	2.8	7.59E-04	9.3E+16	2.87E+05	16.97000	6.92E+07	3
11.6	9.28	5.49E-02	16.5	2.9	7.05E-04	8.7E+16	2.87E+05	16.93813	6.33E+07	2
12	9.42	5.33E-02	16.0	3	6.57E-04	8.1E+16	2.87E+05	16.90738	5.82E+07	2
12.4	9.56	5.19E-02	15.6	3.1	6.13E-04	7.5E+16	2.88E+05	16.87768	5.36E+07	2
12.8	9.69	5.05E-02	15.2	3.2	5.74E-04	7.1E+16	2.88E+05	16.84896	4.95E+07	2
13.2	9.82	4.93E-02	14.8	3.3	5.39E-04	6.6E+16	2.88E+05	16.82116	4.58E+07	2
13.6	9.95	4.81E-02	14.4	3.4	5.06E-04	6.2E+16	2.88E+05	16.79422	4.26E+07	2
14	10.08	4.69E-02	14.1	3.5	4.77E-04	5.9E+16	2.88E+05	16.76808	3.96E+07	1
14.4	10.20	4.58E-02	13.7	3.6	4.50E-04	5.5E+16	2.89E+05	16.74271	3.69E+07	1
14.8	10.33	4.48E-02	13.4	3.7	4.25E-04	5.2E+16	2.89E+05	16.71805	3.45E+07	1
15.2	10.45	4.38E-02	13.1	3.8	4.02E-04	4.9E+16	2.89E+05	16.69408	3.23E+07	1
15.6	10.56	4.29E-02	12.9	3.9	3.81E-04	4.7E+16	2.89E+05	16.67074	3.03E+07	1
16	10.68	4.20E-02	12.6	4	3.62E-04	4.4E+16	2.89E+05	16.64802	2.84E+07	1
16.4	10.79	4.12E-02	12.3	4.1	3.44E-04	4.2E+16	2.89E+05	16.62587	2.67E+07	1
16.8	10.91	4.03E-02	12.1	4.2	3.27E-04	4.0E+16	2.89E+05	16.60428	2.52E+07	1
17.2	11.02	3.96E-02	11.9	4.3	3.11E-04	3.8E+16	2.90E+05	16.58320	2.38E+07	1
17.6	11.13	3.88E-02	11.6	4.4	2.97E-04	3.7E+16	2.90E+05	16.56263	2.24E+07	1
18	11.23	3.81E-02	11.4	4.5	2.84E-04	3.5E+16	2.90E+05	16.54253	2.12E+07	1
18.4	11.34	3.74E-02	11.2	4.6	2.71E-04	3.3E+16	2.90E+05	16.52288	2.01E+07	1
18.8	11.44	3.68E-02	11.0	4.7	2.59E-04	3.2E+16	2.90E+05	16.50366	1.91E+07	1
19.2	11.55	3.61E-02	10.8	4.8	2.48E-04	3.1E+16	2.90E+05	16.48487	1.81E+07	1
19.6	11.65	3.55E-02	10.7	4.9	2.38E-04	2.9E+16	2.90E+05	16.46646	1.72E+07	1
20	11.75	3.49E-02	10.5	5	2.28E-04	2.8E+16	2.90E+05	16.44844	1.64E+07	1

TOTAL COLLISIONS = 306

L > 0.9 mm

photodissociation fluxes are required to produce ten counts per laser pulse at the signal averager. Hence all three of the design criteria for the nozzle have been satisfied for this configuration. The $H_2(B)$ collision frequency is shown in Fig. 7 as a function of expansion distance. The $H_2(B)$ radiative rate is given by the dashed line. This confirms that excitation at distances less than 0.9 mm are required for $H_2(B)$ quenching to dominate over radiative decay.

The molecular beam source we have chosen for our application is manufactured by Newport Research Corporation (Model BV-100/BV-100D). This is the commercial version of a design by Adams and coworkers[19] and is shown schematically in Fig. 8. The valve operates at stagnation pressures up to 10 atm with a pulse duration as low as 100 µs and a repetition rate of 50 Hz.

A-4608
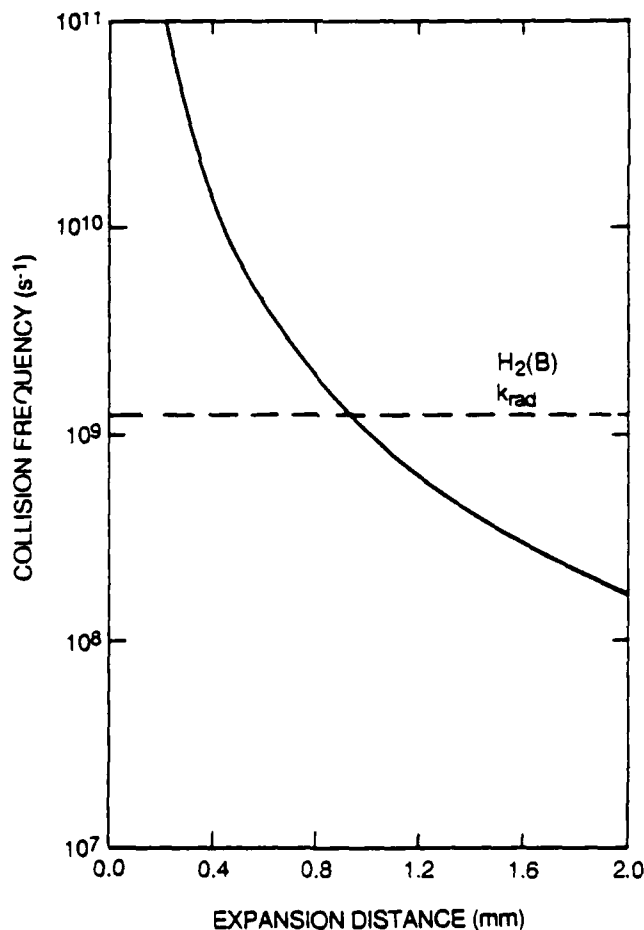
Figure 7. $H_2(B)$ collision frequency as a function of distance from the nozzle throat.

12
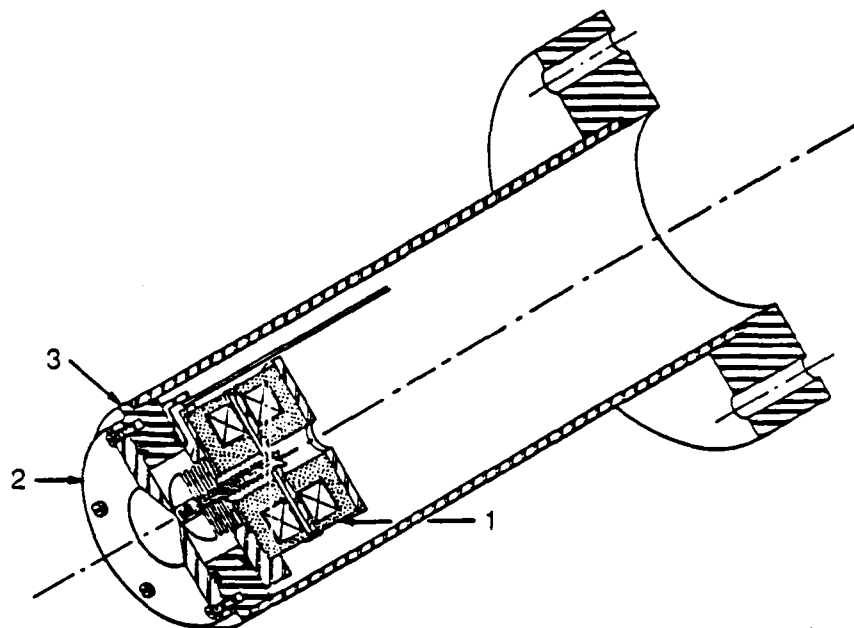
A-4612

Figure 8.   Cutaway view of solenoid-actuated pulsed beam source (Adams et al., 1981). (1) Actuator assembly with dual solenoids and ferrite cores. (2) Nozzle plate. (3) Mounting ring.

1.2.2 Discharge Excitation

Discharge excitation of Ar^* in Ar/H_2 mixtures was accomplished using the throat-discharge modifications to the NRC pulsed beam valve as described by Grant and coworkers[20] and further modified by Physical Sciences Inc. (PSI). These modifications are shown in Fig. 9. The basic concept involves the passage of the expanding gas through a region between two biased plates. The two plates are separated by a ceramic insulator. Grant and coworkers experienced a problem with feedback from the discharge affecting the pulsing electronics for the nozzle. To eliminate this problem, a second ceramic insulator was placed between the discharge plate and the nozzle. This isolates the discharge ground from the nozzle and eliminates most of the feedback problems. At higher discharge voltages, feedback in the form of double pulsing of the nozzle was still a problem. Discharge voltage was always increased while monitoring the pulsing signal to the nozzle. If a second pulse was observed, then the voltage was decreased until the nozzle operated normally.
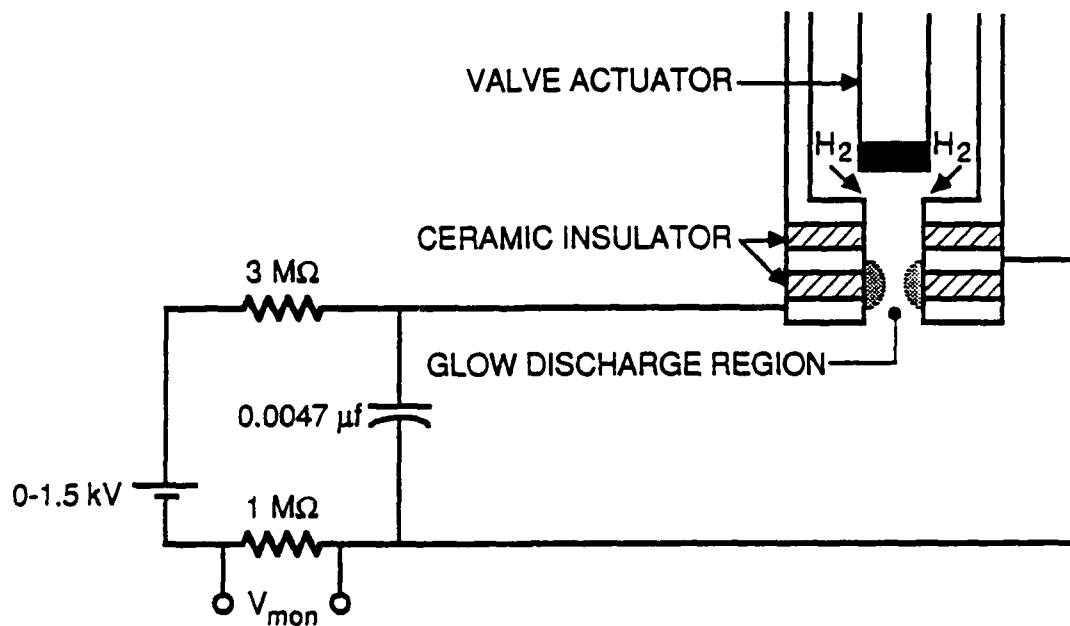
Figure 9. Molecular beam valve with hollow cathode discharge excitation.

When the gas nozzle is closed, the pressure is sufficiently low that no discharge occurs between the plates. As the valve opens and gas fills the void between the plates, initially spark breakdown occurs between the plates and then, as the pressure increases, a transition to glow discharge conditions occurs. Each of these conditions has been treated extensively by Cobine[21] for the case of breakdown between plane parallel electrodes. Our discharge configuration is different, but it is useful to carry out these calculations to roughly parameterize these conditions.

Sparking voltages for H_2 as a function of pressure times distance are shown in Fig. 10. For our gap distance of 3 mm, it can be seen that only modest voltages are required to cause the gas to arc early in the expansion. Extrapolation of the H_2 curve in Fig. 10 to background conditions (pd = 3 x 10^{-4} Torr-cm) shows that very large voltages are required to cause arcing under these conditions.

14
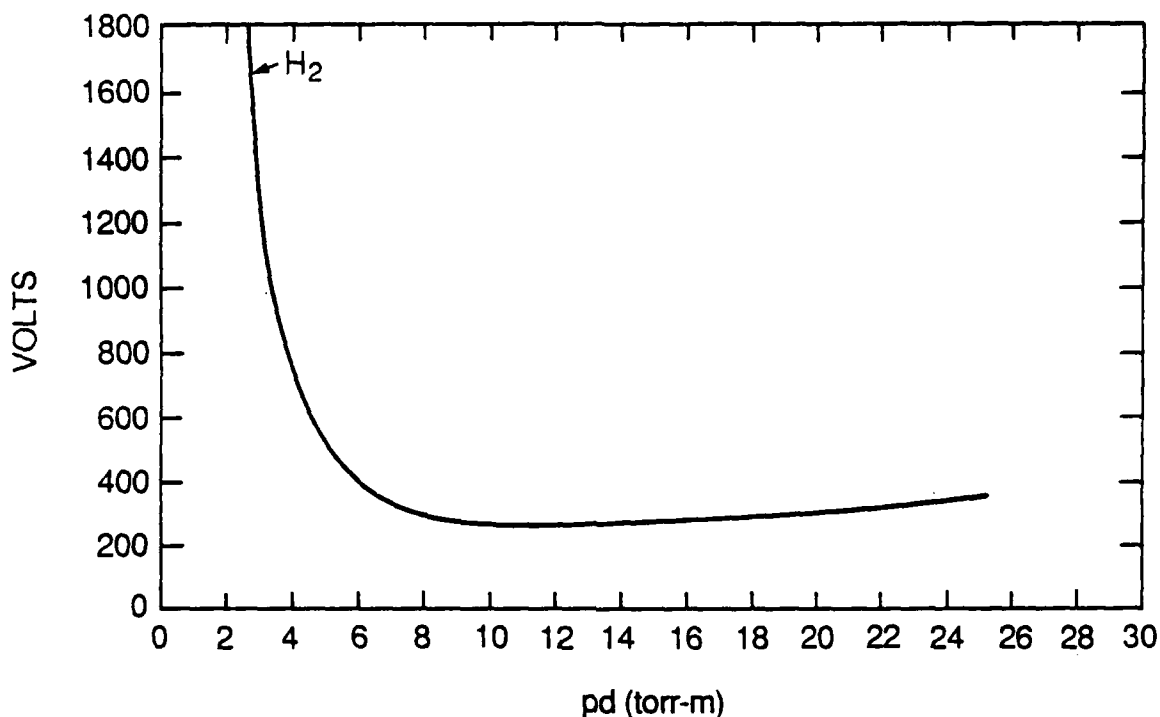
A-4613

Figure 10. Paschen curves for H_2, CO_2, and air.

The transition to glow discharge operation occurs when the gas pressure exceeds the voltage required for arcing. At this point, the gap voltage must be sufficient to sustain a glow discharge. The condition for sustaining a glow discharge is given by:

$$\gamma(e^{\alpha d} - 1) = 1 \tag{9}$$

where α is the coefficient for field-intensified ionization by electrons, γ is the probability for electron production at the cathode from positive ion bombardment, and d is the gap spacing in cm. The coefficient α is a function of pressure and gap voltage. A plot of α/P (cm^{-1} $Torr^{-1}$) as a function of E/P (V cm^{-1} $Torr^{-1}$) is shown in Fig. 11 for H_2, the dominant component in the Ar/H_2 expansion. The value of γ is relatively insensitive to voltage for slow moving ions and has a value of 0.053 for Ni electrodes.[21] Expression (9) can be solved for this value of γ and d = 0.3 cm to give a value of α = 9.96 cm^{-1} to

15
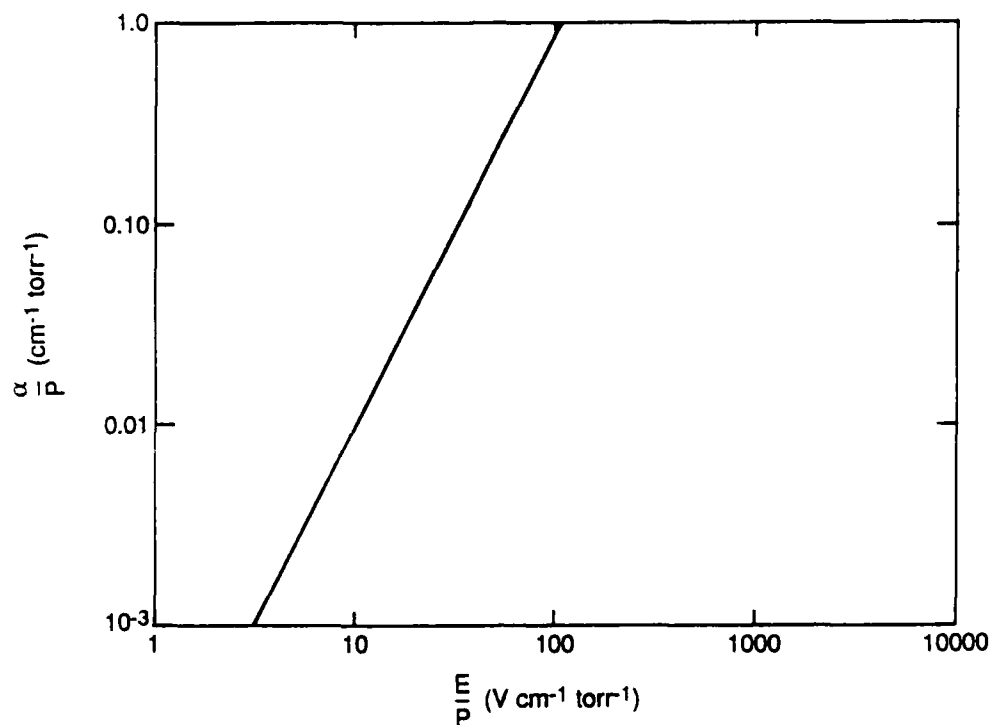
Figure 11. Coefficient of field-intensified emission for H_2.

sustain the glow discharge. Using the curve of Fig. 11 and the range of stagnation pressures possible for use in the valve, the plot of minimum bias voltage versus gap pressure shown in Fig. 12 is obtained. In the discharge excitation experiments, the discharge is conducted in the throat region and stagnation pressures as low as 0.4 atm may be employed to achieve the required collision frequency at the point of $H_2(B)$ formation. Under these conditions, a bias voltage of 1.5 kV is required to sustain the discharge.

The glow discharge current is limited to a few hundred microamps by placing a 3 MΩ ballast resistor in series with the spark gap and the power supply. The two parallel discharge plates have a calculated capacitance of 4.7 pf. A 0.0047 μf capacitor was added in parallel to increase the total capacitance of the discharge circuit. The ability to monitor the discharge was accomplished by adding a 1 kΩ resistor in series with the voltage. We could then determine when the discharge fired reproducibly under various conditions.
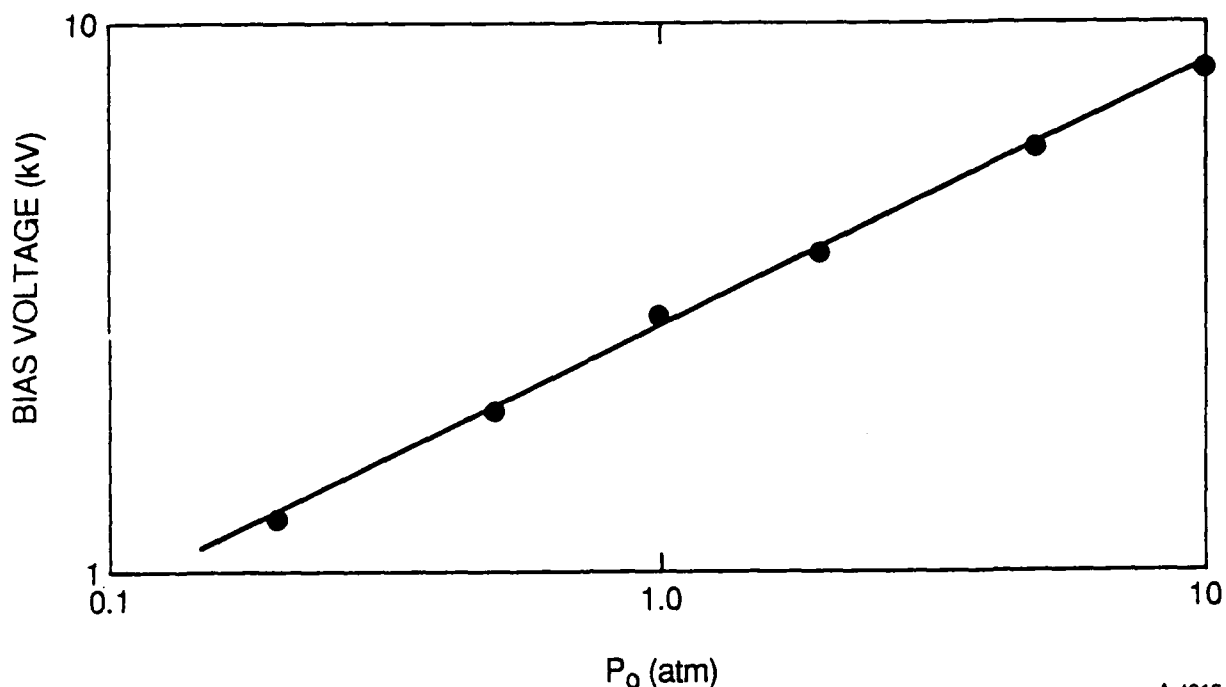
Figure 12. Minimum gap voltage required for sustained glow discharge in H_2 as a function of nozzle stagnation pressure.

1.2.3 Discharge Characterization

The gas valve is fired through an internally generated pulse. The discharge then self-fires as the gas pressure increases between the two plates. Under these conditions, the discharge pulse has a 2 μs duration. This is considerably shorter than the several hundred microseconds the valve is open. There is also 50 μs of firing jitter between the pulse that fires the gas valve and the firing of the discharge. Attempts to reduce the jitter by adjusting discharge voltage, gas pressure and repetition rate were unsuccessful. To eliminate the jitter from our detection electronics, the signal from the discharge monitor was used as a trigger source.

Since the discharge pulse is shorter than the valve gas pulse, the question arises as to when in the gas pulse the discharge is firing. The gas valve is a solenoid valve requiring 50 μs to open fully and reach full gas pressure at the

17

throat. If the discharge fires before the valve fully opens, then the concentration of H_2 could be considerably less than what is required for quenching of $H_2(B)$.

A discharge voltage of ~380V was needed to achieve breakdown. The discharge was operated at 700 to 800V for a pure H_2 discharge. A slightly lower voltage was needed for H_2/Ar mixtures to prevent feedback to the pulsed valve. The discharge proved to be fairly insensitive to pressure which could indicate the discharge fires before the valve fully opens. A pressure of 400 Torr was used to assure a H_2 concentration large enough to quench $H_2(B)$.

The question arises as to whether we ever achieved glow discharge or only created a spark discharge. We calculated a voltage of 1.5 kV was required for glow discharge at 400 Torr of hydrogen. However we could not operate at this voltage because of feedback problems. If the valve was not opening completely before discharge, the actual pressure would be less than 400 Torr and a glow discharge formed. The pressure insensitivity of the discharge would indicate that this might be true for our operating conditions.

1.2.4 Detection of H_4^*

Detection of H_4^* was attempted via observation of passive emission from the excimer and via photodissociation to form $H_2(B)$. Passive emission could be observed using either a vacuum monochromator system (Acton Research Model VM-502) or an N_2-purged broadband radiometer (130 to 190 nm). Nicolaides[5-7] and coworkers have calculated the binding energy of H_4^* to be 3.1 eV with respect to $H_2(B)$ and $H_2(X)$ products. Since the energy of $H_2(B)$ is about 11.7 eV, the excimer might be expected to emit at energies less than 8.6 eV or 145 nm. These wavelengths may be easily observed with an N_2-purged mono-chromator system. A Deslandres table for the H_2(B-X) transition is shown in Table 2. Correlation of the wavelengths in this table with the Franck-Condon factors for the transition calculated by Spindler[22] shows that emission from $H_2(B)$ excited at the nozzle throat will also be observable using this detection system. We can use this emission as a diagnostic to determine when we are in

18

TABLE 2. Deslandres table giving wavelengths in nm for H2(B-X) transitions.

					H2(B,V')				
	0	**1**	**2**	**3**	**4**	**5**	**6**	**7**	**8**
0	110.960	109.264	107.755	106.327	104.973	103.689	102.470	101.314	100.217
1	116.222	114.468	112.813	111.249	109.768	108.365	107.034	105.773	104.579
2	121.778	119.854	118.041	116.329	114.711	113.179	111.729	110.356	109.056
3	127.517	125.408	123.425	121.535	119.789	118.120	116.541	115.047	113.635
4	133.417	131.111	128.944	126.904	124.981	123.165	121.449	119.828	118.297
5	139.448	136.931	134.569	132.349	130.258	128.287	126.427	124.671	123.015
6	145.567	142.826	140.259	137.849	135.582	133.448	131.436	129.540	127.752
7	151.717	148.742	145.960	143.352	140.902	138.598	136.430	134.387	132.465
8	157.823	154.606	151.602	148.791	146.153	143.676	141.347	139.156	137.096
9	163.791	160.329	157.101	154.084	151.257	148.606	146.115	143.775	141.577
10	169.508	165.803	162.353	159.133	156.1??	153.296	150.648	148.162	145.828
11	174.839	170.900	167.237	163.822	160.631	157.544	154.844	152.219	149.757
12	179.633	175.478	171.618	168.024	164.669	161.531	158.593	155.840	153.260
13	183.724	179.380	175.34.	171.598	168.100	164.831	161.773	158.909	156.228
14	186.941	182.445	178.277	174.401	170.789	167.416	164.262	161.310	158.548
15	189.117	184.517	180.255	176.294	172.603	169.159	165.939	162.928	160.111
16	190.103	185.456	181.150	177.150	173.??5	169.948	166.698	163.660	160.817
17	189.783	185.151	180.859	176.872	173.158	169.692	166.452	163.422	160.588
18	188.085	183.554	179.316	175.396	171.743	168.332	165.144	162.161	159.370

H2(X,V")

resonance with H_2(B-X) transitions as well. A lens system was used to image
the H_2 beam centerline on the monochromator slits for improved signal strength.

A boxcar signal averager was employed to record the signal from the
monochromator system.

1.2.5 Overall Chamber Design

The vacuum chamber was comprised of an 8 in. diameter four-way cross (Fig. 13)
mounted on a diffusion pump stack. The diameter of the cross is matched to the
diffusion pump throat to minimize conductance losses through the chamber. The
pumping system consists of an 8 in. diffusion pump (Varian VHS-6), a liquid N_2
cooled cryotrap (Varian 316), and an aluminum slide valve. The total through-
put of the system is 2040 ls^{-1}. All joints in the system are either ASA o-ring
or knife-edge flanges. The molecular beam valve is directed horizontally in
the chamber. Eight ports located symmetrically around the nozzle can be used
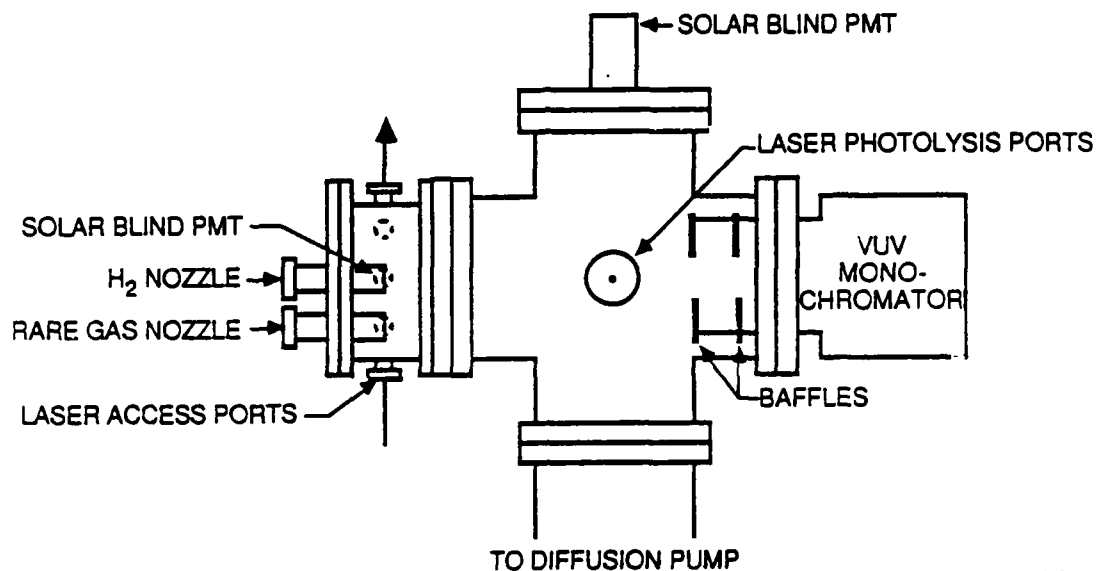
Figure 13. Schematic diagram of H_4^* apparatus.

for laser access and detection of $H_2(B)$ for H_4 fluorescence with a solar blind photomultiplier. To resolve the fluorescence, a vacuum ultraviolet monochromator is attached to the end of the vacuum chamber opposite the pulsed nozzle. A CaF_2 lens is used to image the throat of the nozzle onto the slit of the monochromator. For our experiments, it was sufficient to purge the monochromator with nitrogen.

1.3 RESULTS

1.3.1 $H_2(B)$ Spectrum

A spectrum of the emission from the discharge region was obtained using the vacuum ultraviolet monochromator and recorded on a computer. A typical spectrum for a pure H_2 discharge is given in Fig. 14. The spectrum was taken with 10Å resolution. A spectral fit to the experimental spectrum is then generated by computer in three steps. First, a very high resolution spectrum

20
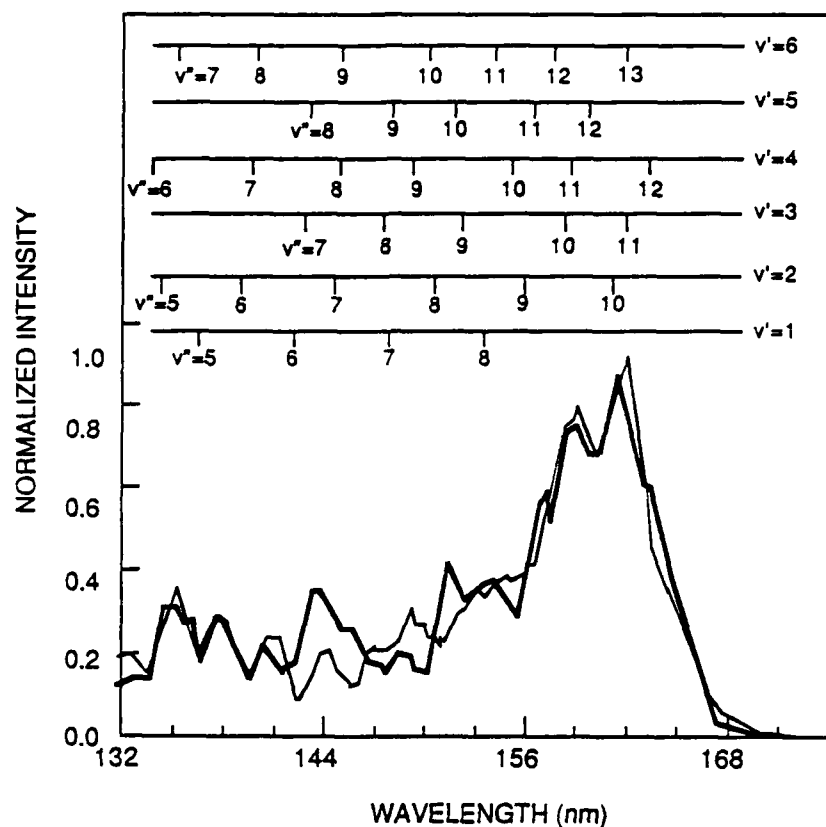
Figure 14. $H_2(B)$ emission spectrum. Thin line represents measured spectrum and thick line is the spectral fit.

covering the wavelength range and vibrational levels needed is generated by calculating the emission intensities and line positions for a given molecular system. Second, vibrational basis sets are generated by passing an appropriate slit function over the high resolution spectrum. Finally, after the data is corrected for instrument response and an average background intensity is subtracted, a least squares fit of the experimental data to the basis functions is calculated. The best fit to the data is given in Fig. 14. A rotational temperature of 1000 K was used to obtain the fit. This is reasonable considering the hot plasma nature of the discharge. Since the resolution of the spectrum is so low, individual vibrational transitions are hard to distinguish. A vibrational distribution can be determined from the spectral fit and is given in Fig. 15. The relative electron excitation efficiency for producing excited

21
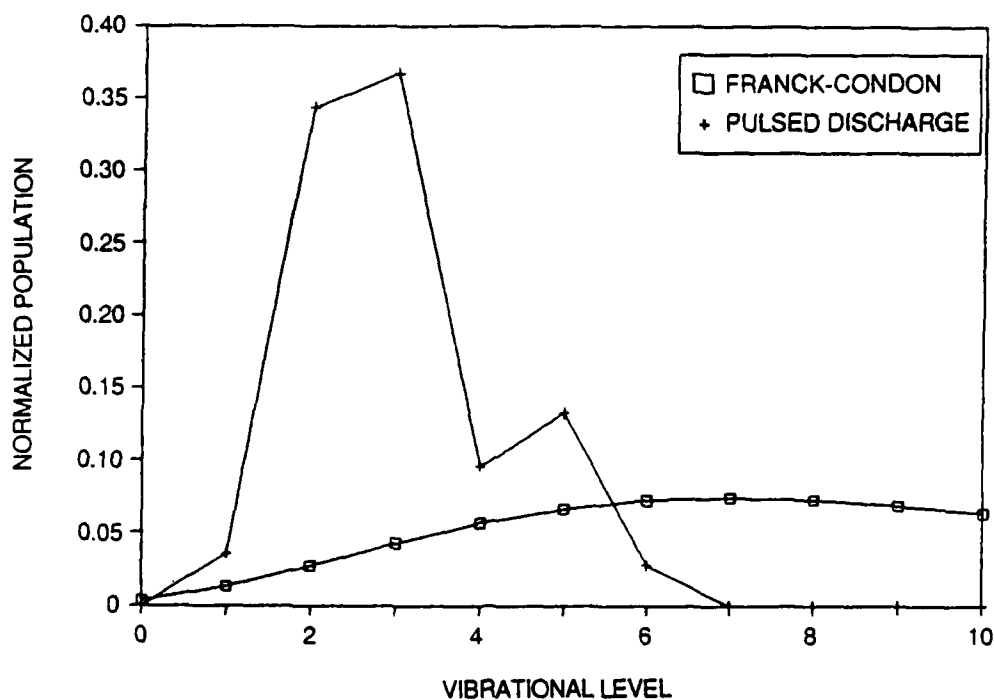
Figure 15. $H_2(B)$ vibrational distribution as determined from calculated spectral fit to experimental spectrum.

$H_2(B)$ is governed by the Franck-Condon factors which connect $H_2(X)$ with $H_2(B)$ in the absence of additional feed mechanisms. The resulting vibrational distribution produced by Franck-Condon type excitation is also given in Fig. 16. The two differ, with the discharge peaking at much lower vibrations. This non-Franck-Condon distribution could be due to vibrational relaxation in the valve throat or an additional production channel of low vibrations. It cannot be accounted for by excitation of $H_2(X,v)$ at a vibrational temperature less than or equal to the electron temperature.

1.3.2 H_2/Ar Mixtures

Additional $H_2(B)$ should be produced by co-discharging H_2 + Ar.

$$Ar + e^- \rightarrow Ar^* + e^- \qquad\qquad (10)$$

$$H_2 + Ar^* \rightarrow H_2(B) + Ar \quad . \qquad\qquad (11)$$

22
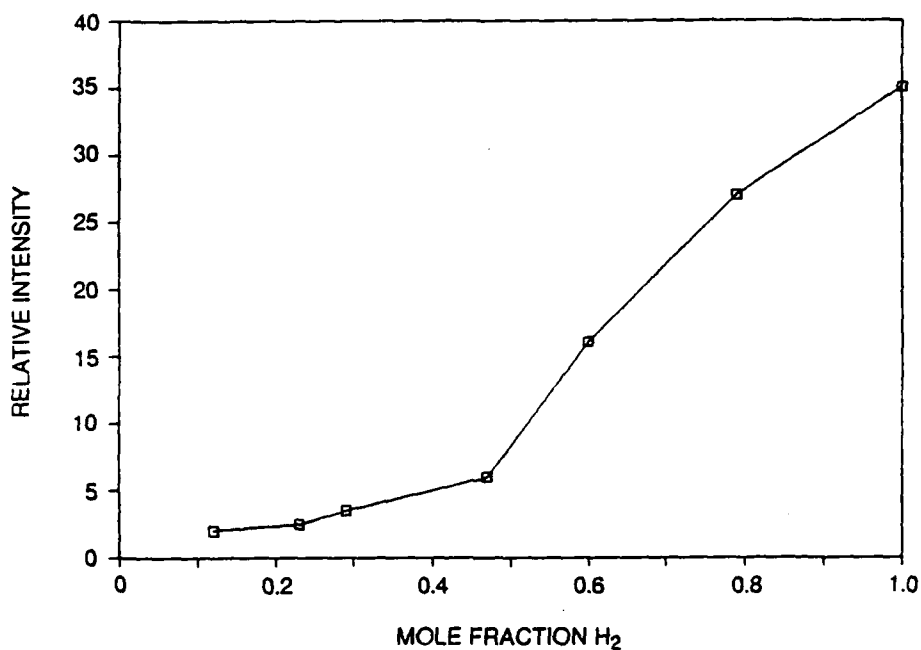
Figure 16. Variation of $H_2(B)$ intensity with variation in Ar/H_2 mixture.

Our calculations have shown that Ar^* will be quenched at similar H_2 concentrations needed to quench $H_2(B)$. Monitoring the $H_2(B)$ fluorescence signal while adding Ar to the discharge mixture, we observed a decrease in the $H_2(B)$ signal. The variation of $H_2(B)$ intensity with varying amounts of Ar is given in Fig. 16. The signal is largest for the pure H_2 discharge, then decreases as Ar is added and finally plateaus at large Ar concentration. No evidence for Ar^* energy transfer to H_2 to form additional $H_2(B)$ was observed. This effect can be explained by considering that we are co-discharging H_2 + Ar. In this system, there is a competition for the available electrons. Any electrons used to form Ar^* are no longer available to produce $H_2(B)$. This electron depletion by argon is much more efficient then energy transfer from Ar^* to H_2.

1.3.3 Atomic Hydrogen

Spectra of the discharge were also recorded in the visible. The spectrum given in Fig. 17 shows several peaks. This can easily be assigned to atomic hydrogen

23
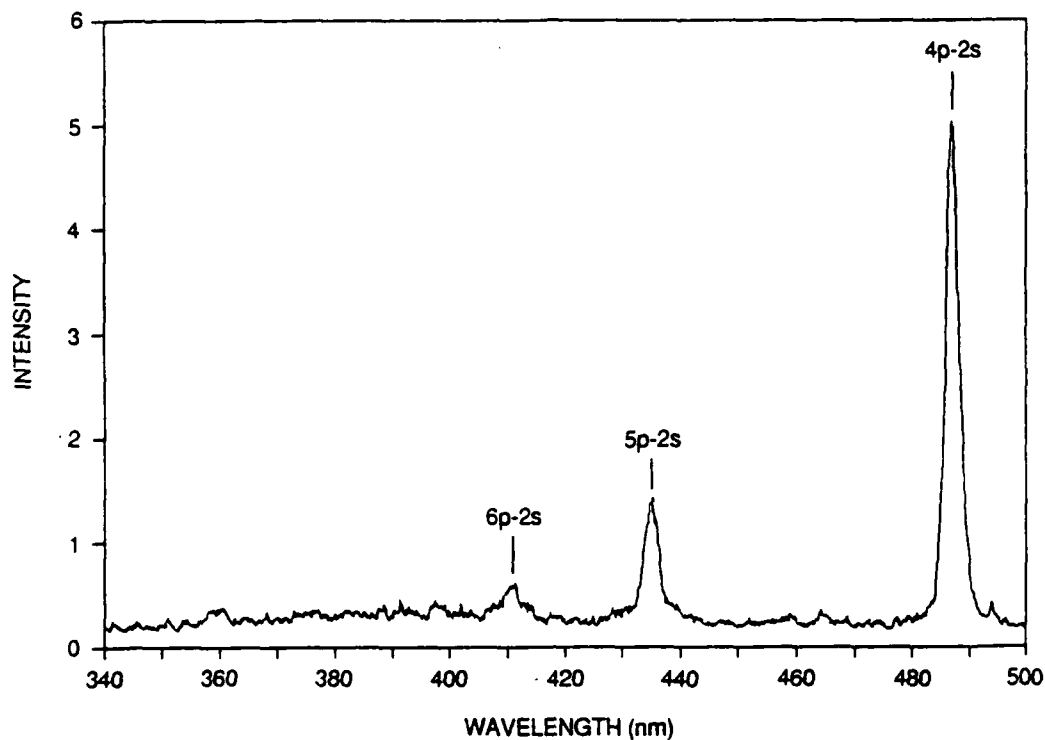
Figure 17. H-Atom emission spectrum from discharge source.

transitions. Since an absolute calibration of our detection system has not
been done, no comparison can be made of the ratio of atomic hydrogen to $H_2(B)$
formed. The quenching rate coefficient of $H_2(B)$ by atomic hydrogen is unknown
but may be an additional depletion channel of $H_2(B)$.

1.3.4 $\underline{H_4}^*$ Production

Formation of stabilized H_4^* is a three-body process. Sufficient collisions
must occur in the post-excitation region between the colliding $H_2(B)-H_2$ complex
and a third body. By forming $H_2(B)$ at the throat of the gas valve, we should
have sufficient collisions. However, if the discharge is firing before the
valve opens fully, sufficient collisions may not occur. After confirming that
$H_2(B)$ was being formed in our discharge source, the next step was to try to
detect the formation of H_4^*.

24

Detection of H_4^* may be via observation of passive emission from the radiating excimer or via photodissociation of H_4^* to produce $H_2(B)$, which may be observed in emission. Emission was detected with a broadband radiometer (130 to 190 nm) or a monochromator (190 to 540 nm). All emission observed from the discharge could be assigned to $H_2(B)$ or atomic hydrogen; no passive emission due to H_4^* was observed.

A nitrogen laser was used for photolysis of H_4^* at 337 nm. The photolysis laser was delayed with respect to the discharge source. Delays of 0 to 30 μs were used, but no $H_2(B)$ emission was observed.

There is a second channel possible for H_4^* photolysis:

$$H_4^* \rightarrow H_3^+ + H^- \quad .$$
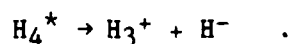
Though we cannot currently detect ions, this channel does need to be examined. However, a different source of $H_2(B)$ would be needed since our discharge source produces ions. A cleaner source, such as laser excitation of $H_2(B)$, would be ideal.

1.3.5 Detection Limits

Since we were unable to observe any signal from H_4^*, it is important to establish detection limits on our system. First we need to calculate the $[H_2(B)]$ formed in our source. This is determined by the electron density of our discharge source, the excitation rate coefficient, and the concentration of H_2. Using the current measured by our current monitor, the electron flux for the discharge area can be calculated to be 1.25×10^{18} e$^-$ cm^{-2} s^{-1}. Ajello et al.[23] have measured the emission cross section of $H_2(B)$ by electron impact over an energy range from threshold to 400 eV. The threshold for this system is 20 eV. In our discharge the average energy is assumed to be 2 eV. The fraction of electrons above threshold is then calculated assuming a Boltzmann distribution. The excitation rate is then the product of the cross section and the fraction of the electrons above threshold. For our operating conditions,

we calculate an excitation rate coefficient of 0.106 e$^-$/s. The concentration of H_2 is 1.29 x 10^{19} molecules cm^{-3}. The production of $H_2(B)$ is then 1.4 x 10^{18} molecules cm^{-3} s^{-1}. The discharge occurs for 2 μs so $[H_2(B)]$ = 3 x 10^{12} molecules cm^{-3}.

The next problem is to determine how much H_4^* will be formed from $H_2(B)$. The relevant equations for this process are:

$$H_2(X) + e^- \rightarrow H_2(B,v) \qquad\qquad j_1 = \sigma I \qquad\qquad\qquad (12)$$

$$H_2(B) + H_2 \rightarrow H_4^* \qquad\qquad\qquad \phi k_2 \qquad\qquad\qquad\quad (13)$$

$$H_4^* + M \rightarrow 2H_2 + M \qquad\qquad\quad k_{-3} \qquad\qquad\qquad\quad (14)$$

$$H_4^* + M \rightarrow H_4 + M \qquad\qquad\quad\; k_3 \qquad\qquad\qquad\quad\; (15)$$

$$H_4^* \rightarrow H_2(B) + H_2 \qquad\qquad\quad\; k_4 \qquad\qquad\qquad\quad\; (16)$$

$$H_2(B) \rightarrow H_2 + h\nu \qquad\qquad\qquad A_5 \quad . \qquad\qquad\qquad (17)$$
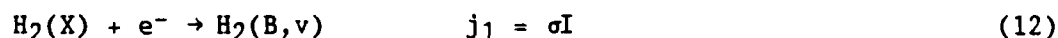
The H_4^* lifetime is very short so a steady-state solution is appropriate:

$$\frac{d[H_4]}{dt} = j_1[H_2] \left\{ \frac{\phi k_2[H_2]}{k_2[H_2] + A_s} \right\} \left\{ \frac{k_3[H_2]}{2k_3[H_2] + k_4} \right\} \quad . \qquad (18)$$

The assumption has been made that k_{-3} = k_3 where k_3 is the lifetime of H_4^*. One can then estimate the H_4^* formation efficiency per $H_2(B)$ and, using $[H_2(B)]$ = 3 x 10^{12} molecules cm^{-3}, calculate an estimated $[H_4^*]$ for a predicted H_4^* lifetime. The results are given in Table 3. The dissociation cross section of H_4^* is uncertain but a reasonable estimate would be 10^{-19} cm^2. For our laser at 337 nm we could dissociate 0.02 percent of the H_4^*. The actual photodissociated volume is 0.2 cm^3. If one assumes that all dissociated H_4 forms $H_2(B)$ then, for an H_4^* lifetime of 10^{-10}s, dissociation would form

26

TABLE 3. Production of H_4^*.

k_3 (s^{-1})	H_4^* Quenching Efficiency	[H_4^*] Produced (molecules cm^{-3})	Estimated $H_2(B) \rightarrow H_4^*$ Branching Ratio
10^{10}	10^{-2}	3×10^{10}	0.02
10^{11}	10^{-3}	3×10^9	0.20
10^{12}	10^{-4}	3×10^8	> 1

2.5×10^7 $H_2(B)$ molecules in 0.2 cm^3. Since we are now in the collisionless regime of the gas jet, only the radiation channel is available. The radiative lifetime of $H_2(B)$ is 1.25×10^9 s^{-1} and the laser pulse duration is 10 ns. This gives a total of 3×10^8 photons. The number of photons can be converted to a current by considering the collection efficiency, transmission of the lens and filter, gain of the photomultiplier and quantum efficiency of the photocathode. For our system 3×10^8 photons would give a signal current of 6.4×10^{-7}A. The signal-to-noise limit of the system is 1×10^{-8}A. Therefore, if the lifetime of H_4^* is shorter than 5×10^{-12}s, we would not be able to detect it. In other terms, if the excited state lifetime of H_4^* is 100 ps, the efficiency for producing H_4^* from quenching of $H_2(B)$ is less than 0.02.

In this argument we have made the major assumption that all dissociating H_4^* forms $H_2(B)$. If this were not true, our detection limit of H_4^* would be even higher, as would our yield estimate.

1.3.6 Summary

The discharge nozzle source does produce $H_2(B)$ at the throat of the nozzle. However, the $H_2(B)$ is formed in several vibrational states and rotationally hot (~ 1000 K). No passive emission from H_4^* was observed. An attempt was made to

photolyze any H_4^* present to form $H_2(B)$. No additional $H_2(B)$ fluorescence due to the photolysis laser was observed.

1.4 QUENCHING OF $H_2(B)$

The goal of this program was to selectively excite $H_2(B)$ in a supersonic jet in such a way as to promote the formation of the H_4^* excimer from collision of $H_2(B)$ with H_2. It is important that the $H_2(B)$ be quenched by H_2 before it can radiate. The radiative rate for the B-state has been measured by Hessler[24] to be 1.25×10^9 s^{-1}. Some limited data exists on the quenching rate coefficient of $H_2(B)$ by HD. Fink, Atkins, and Moore[8] give a super-gas-kinetic quenching rate coefficient of 1.1×10^9 cm^3 molecule^{-1} s^{-1} at 300 K.

In this study we have measured the quenching rate coefficient for $H_2(B)$ $v'=3$ and $v'=4$. For each vibrational level we have measured the quenching rate coefficient for several different rotational levels.

In the calculations of Nicolaides et al.,[6] they predict that the stable excited state of H_4 is produced only when the H_2 B-state precursor has sufficient "ionic" character for reaction with $H_2(X)$. This is predicted to occur for $v > 3$ in the upper state. With laser excitation of H_2, we can produce $H_2(B)$ in a single vibrational level. However, there is the possibility of vibrational relaxation. Therefore we have examined whether any vibrational relaxation occurs during quenching.

1.4.1 Experimental Apparatus

$H_2(B)$ is formed by three-photon laser excitation of H_2. The fluorescence from $H_2(B)$ is then measured as a function of hydrogen pressure. The apparatus used for the quenching measurements is shown in Fig. 18. Laser light of the proper wavelength is generated by a Nd:YAG laser pumping a tunable dye laser, which is then frequency doubled. The laser light is then focused into a vacuum cell containing a known pressure of hydrogen. To resolve the $H_2(B)$ fluorescence, a vacuum monochromator with a solar-blind photomultiplier (EMR Photoelectric Model
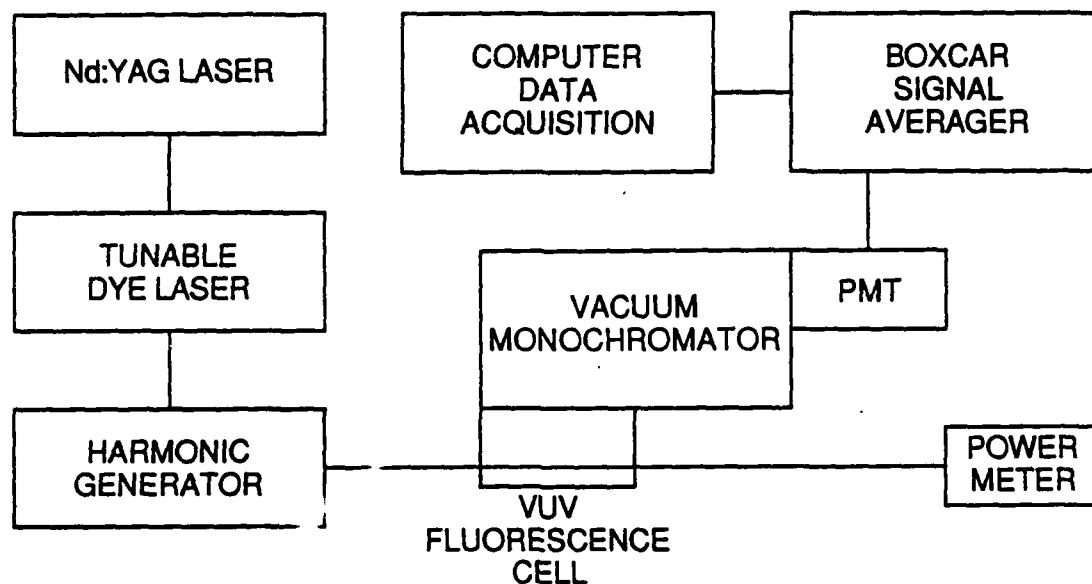
Figure 18. Schematic of $H_2(B)$ quenching experimental apparatus.

542G) is used to detect the signal. The photomultiplier is attached directly to the cell when total fluorescence detection is desired. The signal is then collected by a boxcar signal averager and stored in a computer for later analysis.

1.4.2 Results

1.4.2.1 Vibrational Relaxation. A three-photon excitation spectrum of hydrogen is obtained by scanning the laser and measuring the total $H_2(B)$ fluorescence signal. A typical spectrum is given in Fig. 19. Alternatively one can set the laser wavelength to excitate a single rotational transition and then scan the monochromator to obtain a resolved-fluorescence spectrum. The spectrum in Fig. 20 was obtained by exciting $H_2(B,v'=3,J=2)$ and resolving the fluorescence signal at a resolution of 40Å. A pressure of 102 Torr of hydrogen was used. Our computer spectral fitting codes were then used to generate a fit to the experimental spectrum, which is also shown in Fig. 20. All features in the
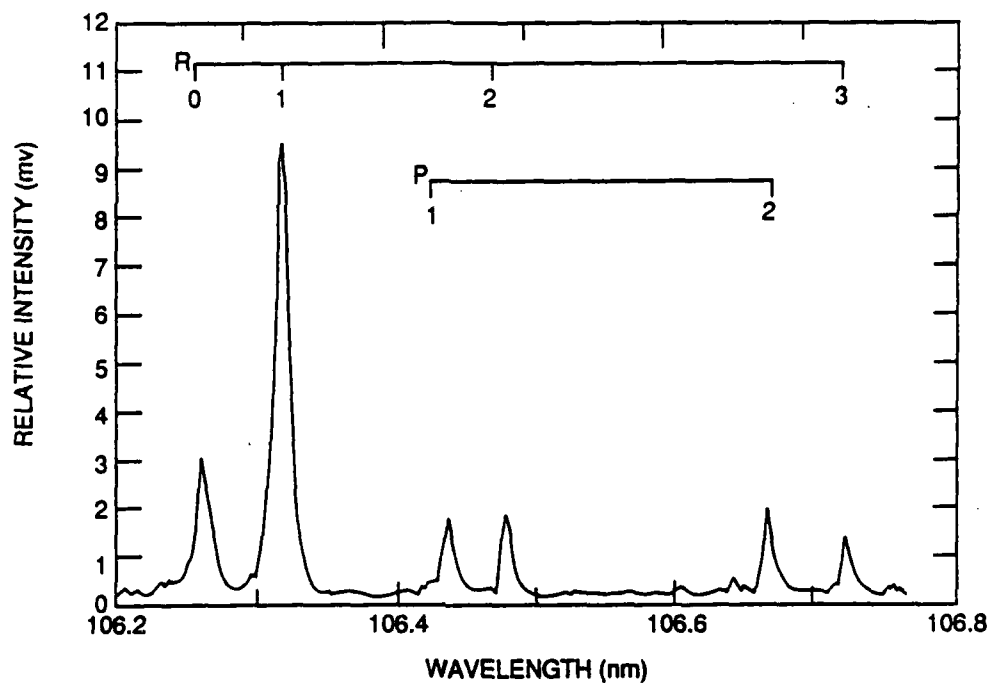
Figure 19.   Three-photon H_2 excitation spectrum. $H_2(B,v'=3) - H_2(X,v=0)$,
80 Torr of H_2.
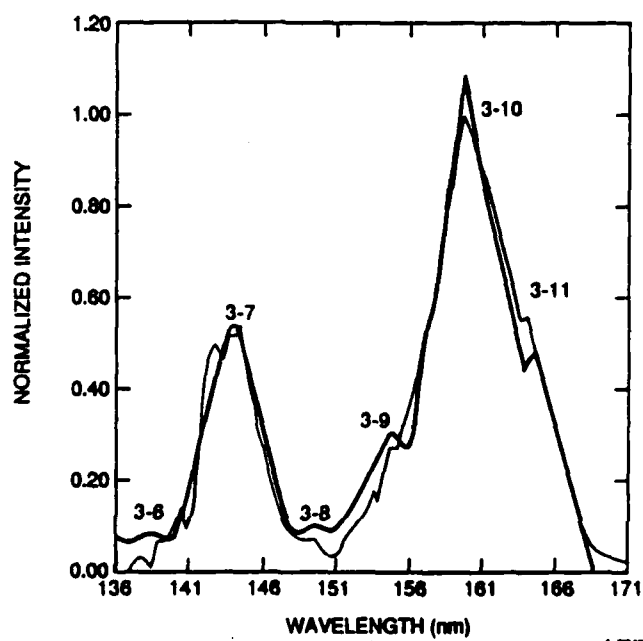
Figure 20.   Excitation of $v'=3$, $J'=2$ transition $H_2(B)$ emission spectrum.
Spectrum taken with 40 Å resolution and 102 Torr of H_2.

spectrum could be assigned to $v'=3$, the vibrational state that was excited by the laser. No evidence for vibrational relaxation was found. Therefore vibrational relaxation is not an important product channel for $H_2(B)$ quenching.

1.4.2.2 Quenching Measurements. To determine quenching of $H_2(B)$ by H_2 the intensity of a single rotational transition was measured as a function of H_2 pressure in the cell. The intensity was then determined by integrating the area under the peak. Use of peak height as an intensity measure was insufficient for two reasons. Pressure broadening of the peak becomes appreciable as the pressure is increased. Therefore, the peak height does not increase as rapidly as the peak area. A second broadening mechanism, stark broadening from the laser field, was also observed.

1.4.3 Kinetic Analysis

The production and depletion of $H_2(B)$ can be summarized in three equations:

$$H_2 + h\nu \text{ (3 photons)} \rightarrow H_2(B,V',J') \qquad\qquad k_1 \qquad (19)$$

$$H_2(B,V',J') \rightarrow H_2(X,V'',J'') + h\nu \text{ (Lyman Bands)} \qquad k_2 \qquad (20)$$

$$H_2(B,V',J') + H_2 \rightarrow \text{Products } (2H_2, \text{ H-Atoms, } H_4{}^*) \qquad k_3 \quad . \quad (21)$$
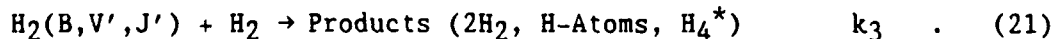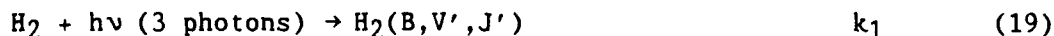
The $[H_2(B)]$ is in steady state during the laser pulse since the radiative lifetime is ten times shorter than the laser pulse duration:

$$\frac{d[H_2(B)]}{dt} = k_1[H_2] - (k_2 + k_3[H_2]) \, [H_2(B)] = 0 \quad . \qquad (22)$$

Substituting $[H_2(B)] = I^*/k_2$ and rearranging, one obtains the equation

$$\frac{[H_2]}{I^*} = \frac{1}{k_1} + \frac{k_3}{k_1 k_2} \, [H_2] \qquad . \qquad (23)$$

To obtain k_3 one plots $[H_2]/I^*$ versus $[H_2]$ where the slope/intercept = k_3/k_2. A typical plot is shown in Fig. 21. This plot is for $H_2(B,v'=3, J'=3)$ quenching and gives a quenching rate coefficient of $13 \pm 3 \times 10^{-10}$ cm^3 molecule^{-1} s^{-1}. A summary of all the quenching rate coefficients determined is given in Table 4. There does not appear to be any significant difference in quenching coefficients for the two vibrational levels for the same J level. There does appear to be some difference between different J levels but, because of the uncertainty in the measurements, it is difficult to determine if a true rotational dependence of the quenching rate coefficient exists. More measurements are needed for different vibrational levels to determine if there is a vibrational dependence of the quenching.

A-7744
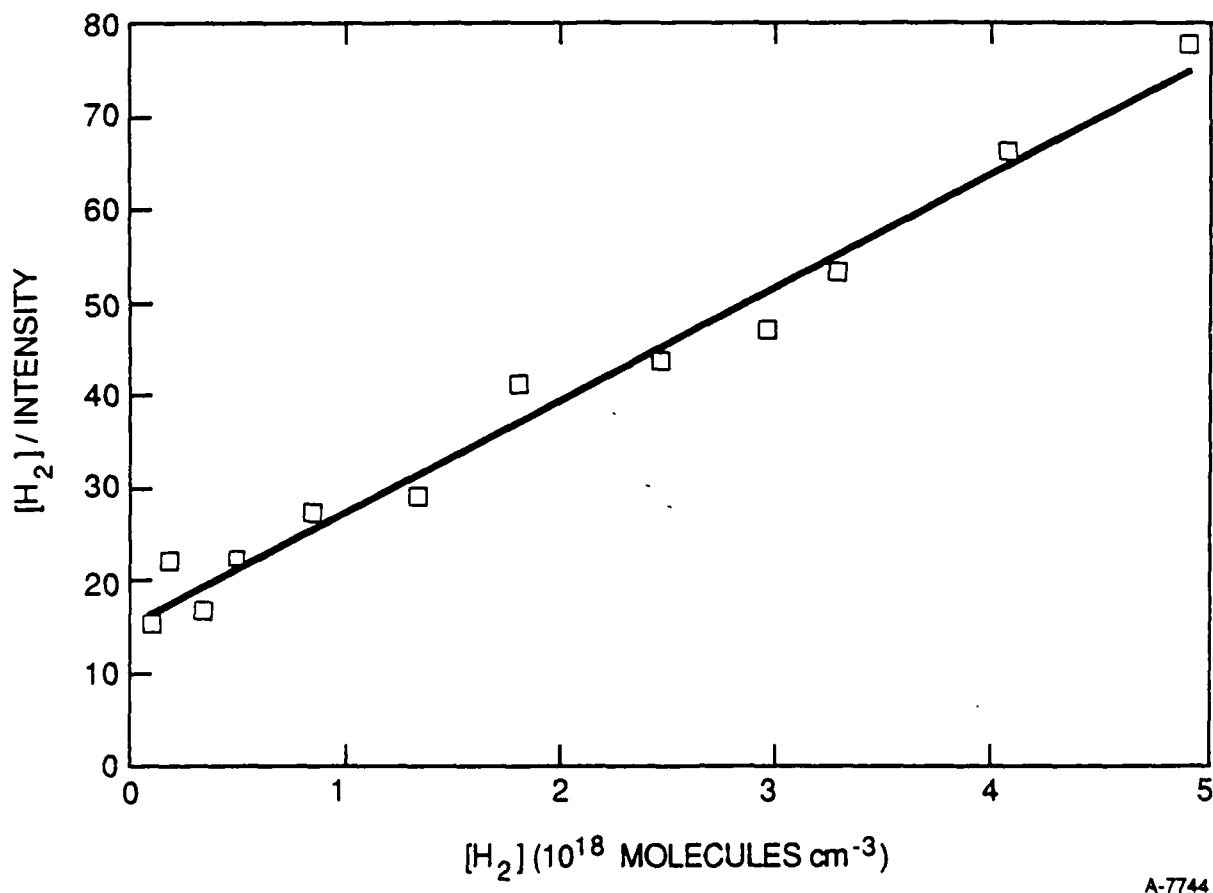
Figure 21. $H_2(B,v'=3, J'=3)$ quenching ($k = 13 \pm 3 \times 10^{-10}$ cm^3 molecules^{-1} s^{-1}).

TABLE 4. $H_2(B)$ quenching rate coefficients.

v	J'	Transition	$k_3(10^{-10}$ cm^3 molecule^{-1} s^{-1})
3	0	P(1)	8.4 ± 1.8
	1	P(2)	13 ± 3
	2	R(1)	15 ± 6
	3	R(2)	13 ± 3
	4	R(3)	5.5 ± 1.5
4	1	P(2)	6.6 ± 1.4
	2	R(1)	13 ± 4
	4	R(3)	4.5 ± 1.0

2. HIGH SPIN NITROGEN

2.1 INTRODUCTION

Experimental investigations of "active" nitrogen have long postulated the existence of a high-energy metastable electronic state of N_2 responsible for the excitation of many species. Various reports indicate the state has a low heterogeneous deactivation probability on glass and metal surfaces and lives for several milliseconds in the gas phase. Matrix isolation studies have shown that chemiluminescence from "active" nitrogen trapped at 10 to 35 K may radiate for many seconds.[25] The existence of such a long-lived metastable state would have important consequences for our understanding of upper atmospheric chemistry, chemical lasers, energy storage and high voltage switching.

Recently, several theoretical efforts have focused on the stability of the "high spin" $^7\Sigma_g^+$ and $^5\Sigma_g^+$ electronic states of N_2. These states arise from the pairing of two $N(^4S)$ atoms to form an N_2 molecule in which all or all but two of the electron spins remain unpaired in the resulting molecular orbitals. These states are characterized by the formation of a weakly-bound (several cm^{-1}) van Der Waals minimum at long r_e and a somewhat more strongly covalently bound minimum at shorter r_e. Since these configurations are the lowest energy of each of the spin multiplicities, they should be stable with respect to decay via dipole radiation and perhaps metastable with respect to collisional deactivation. Curve-crossing to the $^5\Sigma$ state has been postulated by Berkowitz, Chupka, and Kistiakowsky[26] as the mechanism for predissociation of the $B^3\Pi_g$ state.

Early calculations on the stability of the $^7\Sigma$ state were conducted by Vanderslice, Mason, and Lippincott[27] and were refined by Meador.[28] They obtained 13.4 and 14.7 cm^{-1} respectively for the depth of the covalent well. Subsequent calculations by Ferrante and Stwalley[29] and Capitelli and coworkers[30] obtained well depths of 43 and 188 cm^{-1} respectively. Recently, Partridge, Langhoff, and Bauschlicher[31] performed SDCI ab initio calculations and obtained a well depth of 21 cm^{-1}.

The potential of the $^5\Sigma_g^+$ state was initially investigated by Mulliken,[32] who predicted a covalent well depth of ~2300 cm^{-1}. Subsequent calculations by Krauss and Neumann[33] predicted a shallower potential with a well depth much closer to 850 cm^{-1}. Siegbahn[34] calculated that D_e was approximately 1450 cm^{-1}. Experimental evidence for the existence of a stable $^5\Sigma$ state is limited to the effects it may have on the predissociation of the $B^3\Pi_g$ and $a^1\Pi_g$ states. The proposition advanced by Berkowitz et al.,[26] that the $^5\Sigma$ state is responsible for these predissociations, is bolstered by the evidence of Carroll,[35] who derived a well depth of 850 cm^{-1} from predissociation and airglow data.

Recently, Partridge and coworkers[36] performed CASSCF/MRCI ab initio calculations on the $^5\Sigma_g^+$ and $^5\Pi_u$ states of N_2. Their calculations for the $^5\Sigma$ state (designated A') revealed a covalent well depth of approximately 3450 cm^{-1} and a van Der Waals minimum with a binding energy of 47 cm^{-1}. A barrier of approximately 500 cm^{-1} with respect to dissociation to form two N(^{4}S) atoms further enhances the stability of the covalently-bound state. Recombining N(^{4}S) atoms, a primary mechanism for formation of the A'-state, must traverse this barrier to enter the covalently bonded well. The potential supports 7 bound vibrational levels with a spacing of approximately 630 cm^{-1}. The potential for the $^5\Pi_u$ state (designated C") was also found to be more deeply bound than previously estimated. The C"-state well depth is calculated to be 10,505 cm^{-1} with a vibrational spacing of approximately 925 cm^{-1}. A potential energy diagram of these states is shown schematically in Fig. 22.

Perhaps the most important result from the Partridge study was the assignment of the previously unassigned Herman Infrared (HIR) band system of N_2 to the C"$^5\Pi_u$-A'$^5\Sigma_g^+$ transition. This assignment was subsequently confirmed by FTIR studies of Huber and Vervloet.[37] The HIR bands are observed in the 650 to 900 nm region as a result of an energy pooling reaction between two $N_2(A^3\Sigma_u^+)$ molecules.[38-40] Emission from the $C^3\Pi_u$ and $B^3\Pi_g$ states is also observed from the energy pooling process. The calculated radiative lifetime of the C"-state is 4.3 µs, similar to the $B^3\Pi_g$-A$^3\Sigma_u^+$ First-Positive bands.[41] The calculated lifetime is in conflict with experimental observations that the ratio of C"/C state emission intensities is unchanged over a pressure range of
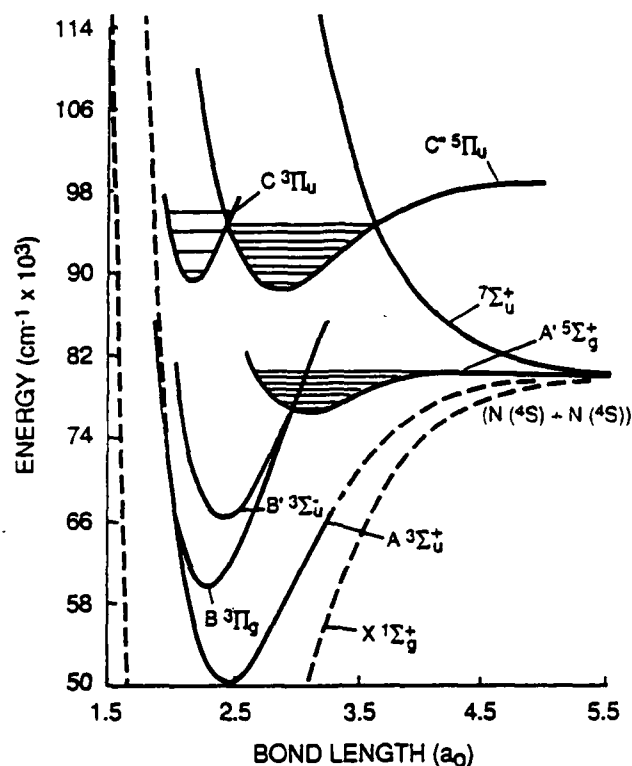
Figure 22. Potential energy diagram for the excited quintet and triplet states of N_2. The vibrational levels of the $C''^5\Pi_u$ and $A'^5\Sigma_g^+$ states are indicated.

a few Torr. This would place the lifetime of the C''-state nearer the 37 ns lifetime of the C-state and raises the possibility that the C''-state derives its lifetime from collisional coupling to the C-state.

The assignment of the N_2 HIR bands to the $C''^5\Pi_u$-$A'^5\Sigma_g^+$ transition coupled with the 3450 cm^{-1} well depth establishes a means of production and indirect evidence for the stability of the A'-state. The 9.45 eV electronic term energy of the A'-state is more than sufficient to excite many of the states observed in "active" nitrogen. However, the magnitude of the intersystem collisional transfer processes and non-radiative spin-orbit and spin-spin couplings to other electronic states in the N_2 manifold, which decrease the A'-state lifetime, have not been addressed. The experiments reported in this section of the report employ laser induced fluorescence and optogalvanic techniques to

quantitatively explore the stability of the A'-state in the gas phase. Several methods of producing the A'-state were explored as part of this effort. The results of these studies are described in the sub-sections which follow.

2.2 EXPERIMENTAL APPROACH

We chose to try three different techniques to form the N_2 (A') state. The first approach was a DC discharge source with optogalvanic detection. Second was an RF discharge source with LIF detection; finally a DC discharge source with LIF detection. Each of these techniques and the results obtained are described in the following three sections.

2.2.1 Optogalvanic Spectroscopy

In optogalvanic spectroscopy a tunable laser is used to probe the spectral characteristics of atomic or molecular species generated in an electric discharge.[42,43] Two conditions are required to generate an optogalvanic signal. First, the laser wavelength must equal a transition of a species present in the discharge. Second, the absorption of energy in the laser beam must alter the impedance of the discharge. There is general agreement that almost all allowed transitions will cause an impedance change and therefore can be detected with optogalvanic spectroscopy. There is less agreement as to the cause of the impedance change. It has been proposed that absorption could alter the concentrations of rare species in the discharge that play a significant role in the dynamics of the discharge. For example, absorption could result in the production of easily ionizable states. In flames it has been observed that the ionization potential of the excited state does influence the magnitude of the impedance change. However, this effect has not been observed in electric discharges. Others attribute the impedance change to an increase in the electron energy. This could cause large local temperature changes to which the discharge is highly sensitive.

The laser induced impedance change can be either positive or negative. The signal is measured by capacitively decoupling the discharge current from the

discharge voltage. The resolution of the optogalvanic spectrum is determined by the laser resolution. The detection sensitivity is limited by the electrical noise of the discharge. For atoms a detection limit of 10^6 atoms cm^{-3} is commonly obtained. The sensitivity for molecules tends to be two to three orders of magnitude lower due to reduced oscillator strengths and distribution of the population over many rotational states.

The optogalvanic spectrum for a pure N_2 discharge has been observed between 570 and 610 nm.[44] The spectrum obtained by Feldmann is shown in Fig. 23. Transitions in the first positive ($B^3\Pi_g$-$A^3\Sigma_u^+$) system and the Ledbetter Rydberg series ($c_4{}^1\Pi_u$-$a''^1\Sigma_g^+$) were observed. Both positive and negative signals were measured. The sign of some of the transitions changed depending on the discharge conditions.
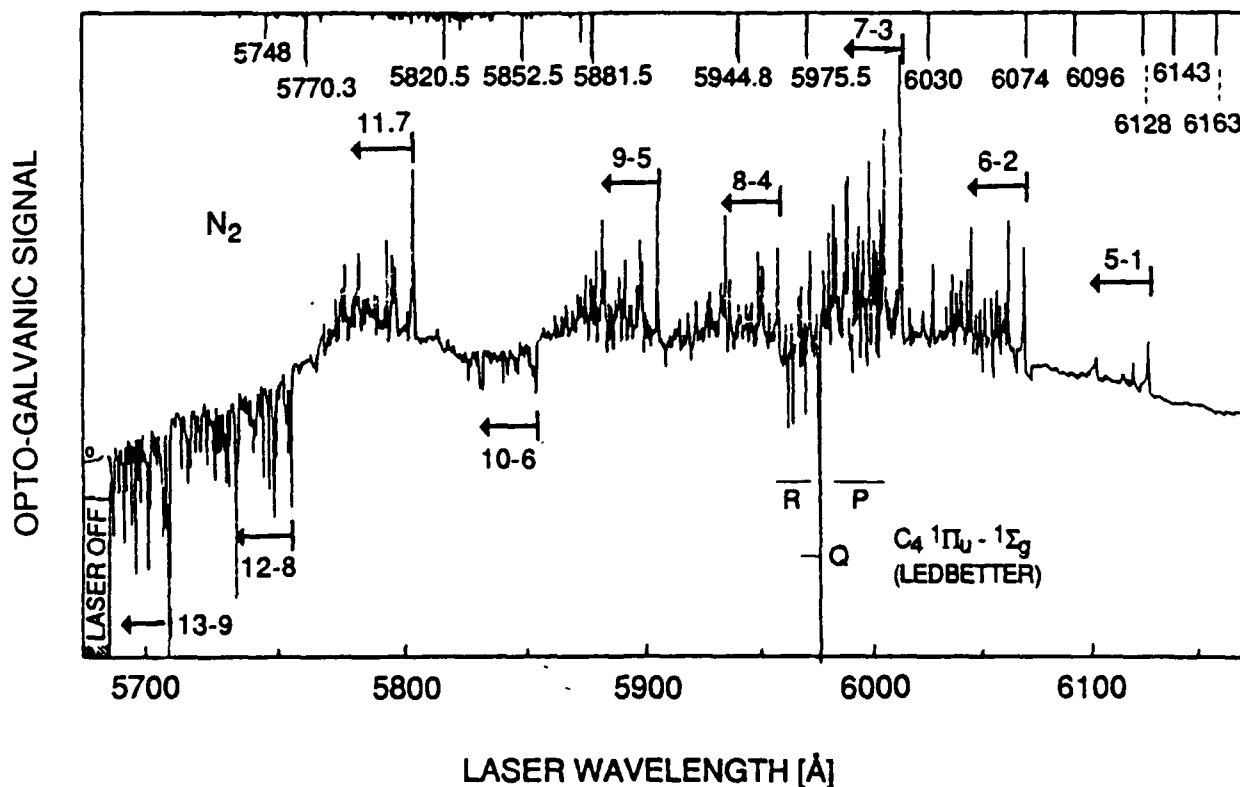
Figure 23. Optogalvanic spectrum of a discharge in N_2. The prominent bandheads of the first positive system are indicated by the respective vibrational quantum numbers. (Ref. 44)

38

Experimental Apparatus

The experimental apparatus is shown schematically in Fig. 24. The flow reactor consists of a 1/2 in. diameter glass tube with a quartz window on each end. Gas enters through a port at one end of the tube and is pumped out at the other end by a 27 cfm mechanical pump. The electrodes are made of tantalum foil. Power is supplied by a high voltage power supply in series with a current limiting resistor. The discharge typically operates at 500V and 1 mA.

Laser excitation is provided by a Quantel system consisting of a YG580 series actively Q-switched Nd:YAG laser pumping a Quantel dye laser. The laser dye LDS698 is used to obtain the needed excitation wavelength. Typical output energies of 30 mJ per pulse are obtained from this laser of a rate of 10 pulses per second. The optogalvanic signal is collected using a gated boxcar integrator. The averaged signal is then stored on a chart recorder or computer. A 0.35m McPherson monochromator with a cooled R943-02 Hamamatsu photomultiplier tube detector is used to obtain a spectrum of the discharge emission. In this way we can verify that $N_2(A)$ is being produced and energy pooling to form the HIR bands is occurring.
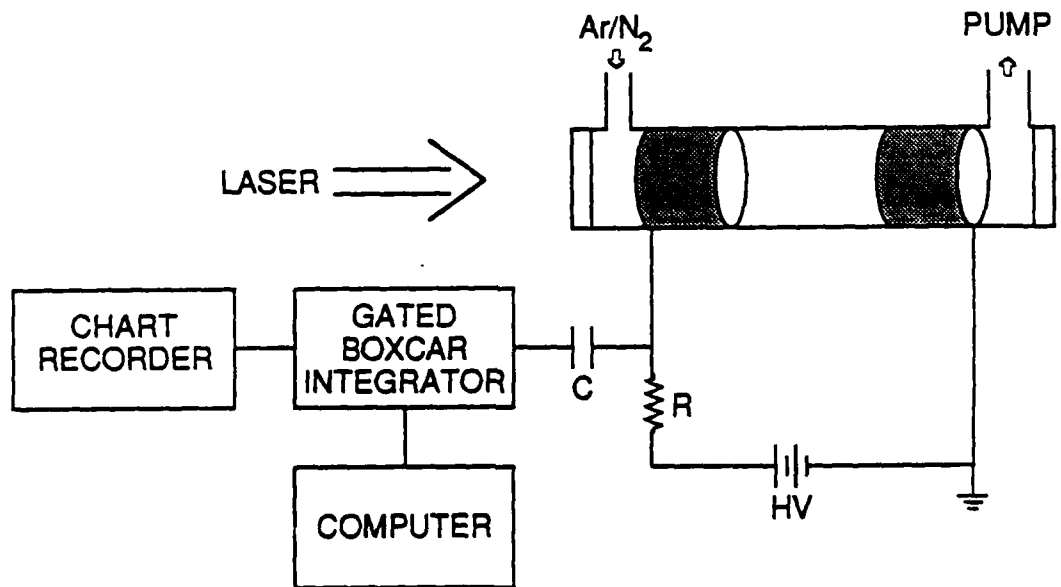
A-8682

Figure 24. Experimental apparatus.

Results

Discharge Emission Spectrum

A portion of the discharge emission spectrum recorded with the monochromator is shown in Fig. 25. Observation of the (3,1) and (2,0) bands of the HIR system is clear evidence that $N_2(A)$ energy pooling is occurring in the discharge. Also observed is emission from the first positive system, $N_2(B^3\Pi_g-A^3\Sigma_u^+)$ and argon metastables. The two HIR bands shown have no overlap with the first positive system and therefore can be observed cleanly. Many of the other HIR bands are obscured under more intense first positive emission. For this reason the region of the (3,1) and (2,0) bands was chosen as the region to probe for optogalvanic signal from the laser.

The rate of C"-state formation may be determined directly via absolute intensity measurements of the HIR bands. The absolute intensities of spectra
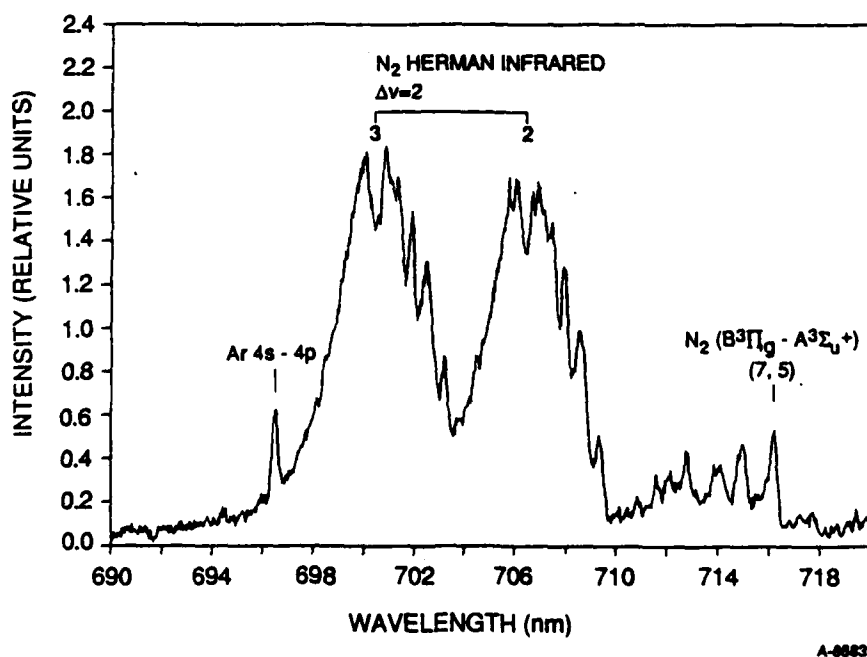
Figure 25. Spectrum of the nitrogen Herman infrared and first-positive system systems excited in the energy pooling of $N_2(A)$ in a nitrogen/argon discharge.

such as Fig. 25 can be integrated to obtain the total intensity of $N_2(C''-A')$,
2-0 and 3-1 bands. Other vibrational levels of the C'' state are not produced
from energy pooling. Since all emission for the C'' state does not occur from
these transitions, the 2-0 and 3-1 band intensities must be corrected for the
fluorescence branching to other lower state vibrational levels in order to
obtain the total emission rates from these levels. Finally, the total emission
intensities from these levels must be summed to get the total HIR formation
rate. The radiative transition probabilities from Langhoff and coworkers[45] are
employed to calculate the fluorescence branching ratios.

The $N_2(C'')$ formation rate based on the intensities of the 2-0 and 3-1 HIR bands
is 7.0×10^{11} molecules cm^3 s^{-1}. This rate is also a lower limit on the rate of
$N_2(A')$ formation, since the A' state may be produced by other mechanisms besides
radiative cascade from the C'' state. The $N_2(A')$ population may be determined if
information about the A' state loss rates are available. Such processes as
collisional quenching and collision-induced predissociation, curve crossing,
radiation, and collisional quenching on the walls must be considered. An upper
limit to the population may be obtained by considering only wall losses.

The time required for a molecule to diffuse from the center of a cylinder to the
walls is given by

$$\tau_d = \frac{r^2}{2.4D} \tag{24}$$

where r is the flow tube radius and D is the diffusion coefficient (~ 30 $cm^2 s^{-1}$
at 6 Torr). The flow tube radius is 1.27 hence the characteristic diffusion
time is 22.4 ms. This is comparable to the residence time of the species in
the flow reactor and hence a steady state solution can be used to obtain the
$N_2(A')$ number density:

$$\frac{d\left[N_2(A')\right]}{dt} = 0 = k_r\left[N_2(C'')\right] - k_D\left[N_2(A')\right] \quad . \tag{25}$$

In this expression, $k_r[N_2(C'')]$ is the radiative rate of $N_2(C'')$, I_{HIR}, and k_D is the inverse diffusion time. Hence, Eq. (25) can be rewritten

$$[N_2(A')] = \frac{I_{HIR}}{k_D} = I_{HIR}\tau_D \quad . \tag{26}$$

Solving Eq. (26) using the HIR intensity and $N_2(A')$ diffusion time quoted above gives an $N_2(A')$ density of approximately 1.6×10^{10} molecule cm^{-3}.

Optogalvanic Spectrum

The excitation laser was scanned over the range 695 to 716 nm and the resulting optogalvanic spectrum was recorded. Many transitions were observed. A second optogalvanic spectrum of a low pressure argon discharge was recorded to aid in distinguishing between argon and nitrogen transitions. Almost all of the transitions observed in the N_2/Ar discharge are also present in the pure Ar discharge. A portion of the spectrum for each discharge is shown in Figs. 26 and 27. The few remaining unassigned lines cannot be readily assigned to any nitrogen transition. They could belong to argon transitions that are too weak under the low discharge conditions of the pure Ar spectrum.

It was impossible to record a pure Ar spectrum at the same pressure as the N_2/Ar discharge because the discharge noise was as large as the signal at higher pressures of pure argon. The discharge noise for the N_2/Ar discharge actually got smaller when the pressure was increased to above 4 Torr. Spectra were recorded under different discharge conditions to determine the effect on the peak intensities. Three spectra taken under different conditions are shown in Figs. 28 to 30. The relative intensities of the three peaks are dramatically different for the three different discharge conditions. The third peak appears as a doublet in the pure Ar spectrum but as only a single peak in the N_2/Ar discharge spectra. Considering the intensity fluctuations that are observed as a function of discharge condition it is possible that all the
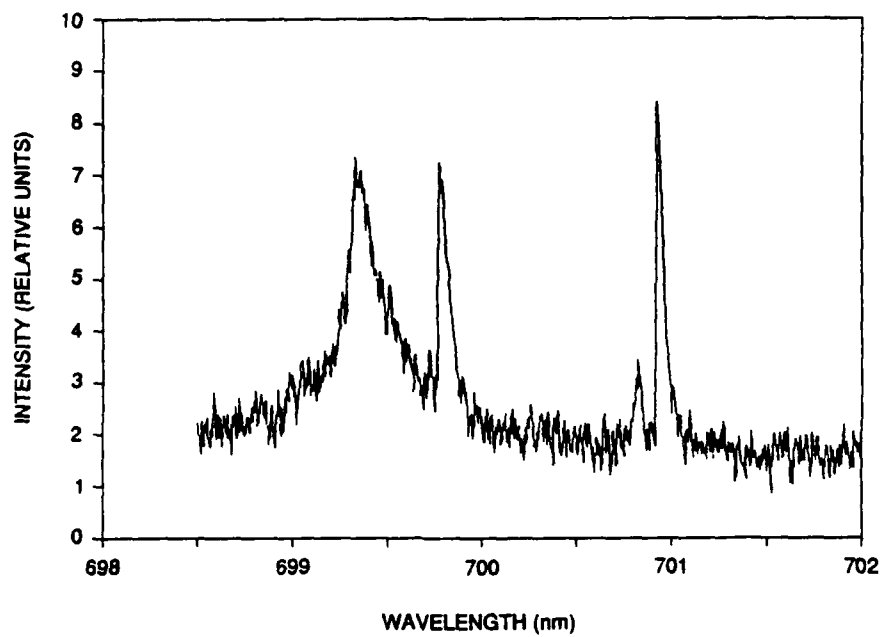
Figure 26.   Optogalvanic spectrum of a nitrogen/argon DC discharge at 4.50 Torr.
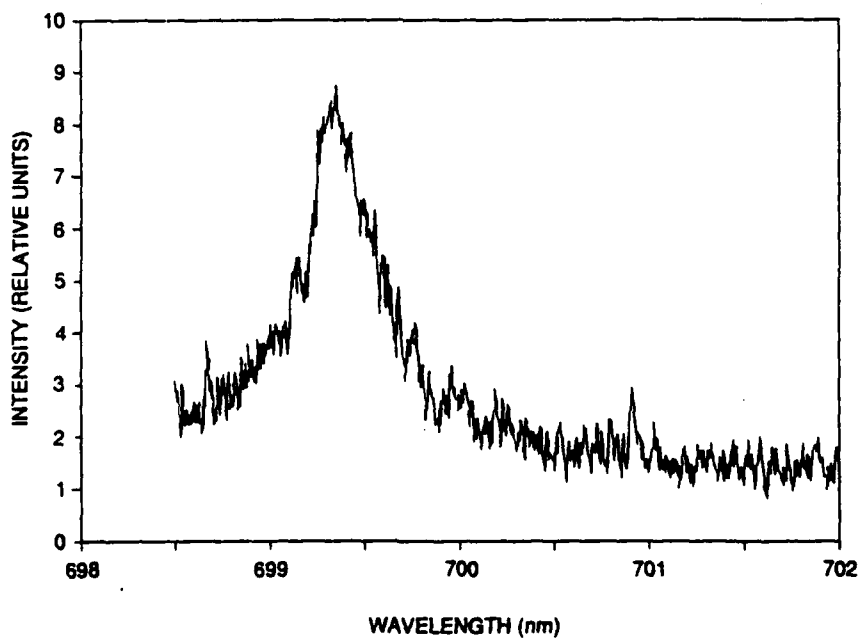
Figure 27.   Optogalvanic spectrum of an argon DC discharge at 0.97 Torr.

43
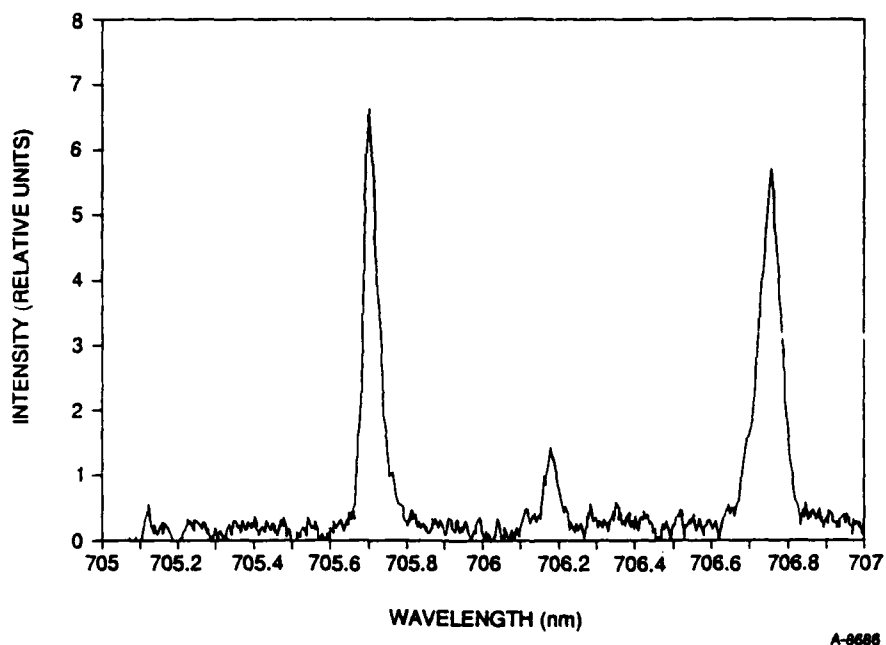
Figure 28. Optogalvanic spectrum of a nitrogen/argon DC discharge at 4.50 Torr.
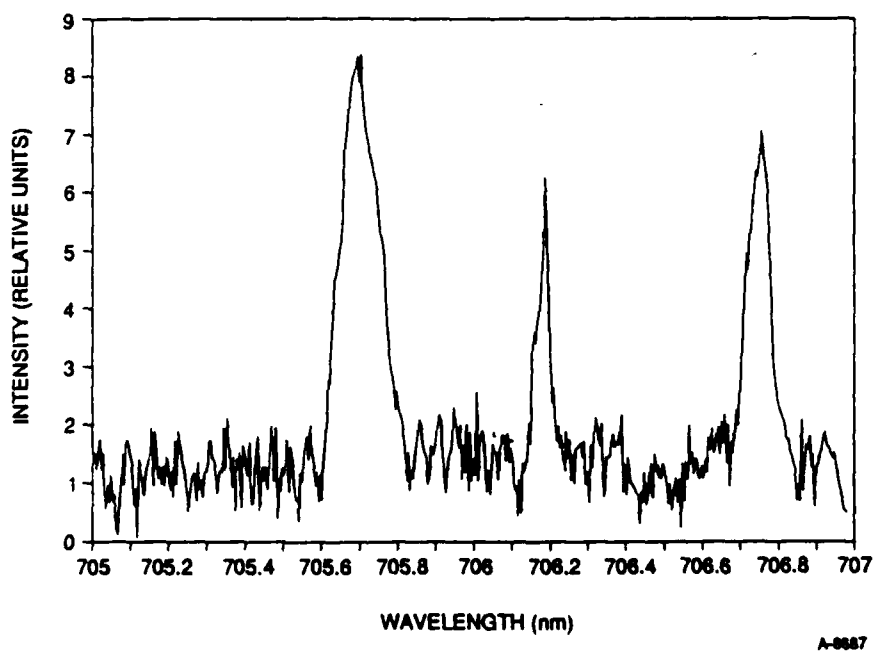
Figure 29. Optogalvanic spectrum of a nitrogen/argon DC discharge at 2.30 Torr.
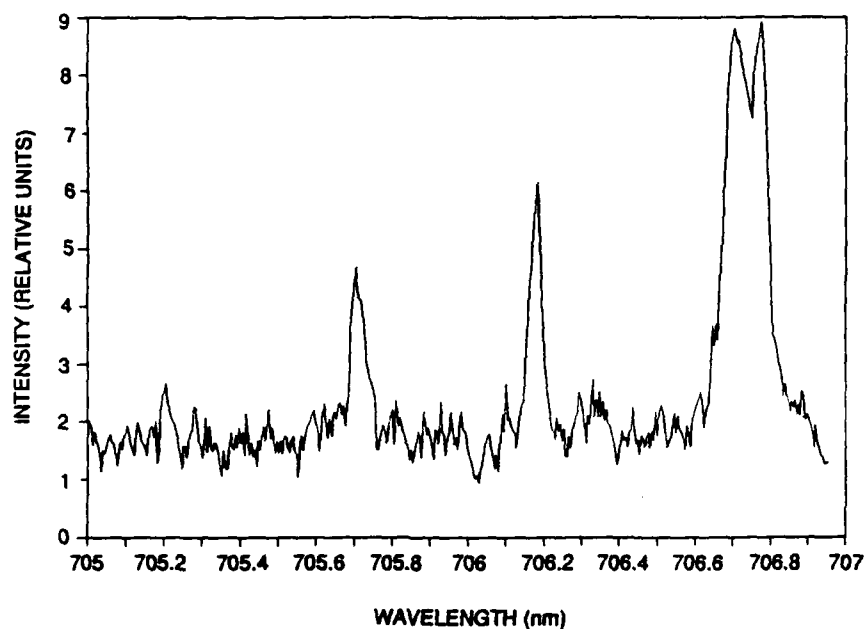
Figure 30. Optogalvanic spectrum of an argon DC discharge at 0.97 Torr.

unassigned lines are argon transitions. There is no real evidence to suggest that any of the transitions observed belong to N_2.

Discussion

The observed emission spectrum confirms that our discharge was operating properly. The observation of HIR emission indicates that the A' state was present in the discharge. Our calculations indicate the A' state may be present at densities approaching 1.6×10^{10} molecule cm^{-3}. However we were unable to observe any optogalvanic signal from any excited N_2. There are several reasons that this might occur. Our discharge source is homemade and was much noisier than expected. Achieving a low noise discharge for optogalvanic spectroscopy appears to be inconsistent with optimal production of the HIR band system. Every gas discharge has a different noise frequency spectrum and methods for reducing noise also vary for each type of discharge.

Previous reports on the sensitivity of optogalvanic spectroscopy with metastable $N_2(A^3\Sigma_u^+)$ indicate that densities as low as 10^8 to 10^9 molecules cm^{-3} may be observed.[44] When we attempted to excite these transitions in our system, we were unable to observe impedence changes corresponding to the $N_2(B^3\Pi_g - A^3\Sigma_u^+)$ First Positive Bands. We estimate the $N_2(A^3\Sigma)$ density to be approximately 3×10^{10} molecule cm^{-3} in this system. Hence, a better estimate of the detection sensitivity under our flow conditions is approximately 10^{10} molecule cm^{-3}. The calculations of Partridge et al.[36] show that B-A and C"-A' have similar oscillator strengths. Our calculations indicate that even modest loss processes would reduce the $N_2(A')$ number densities expected in our system below the rough detection limit for these particular experiments. Hence, it is quite likely that the A'-state is produced quite efficiently under our conditions but that optogalvanic spectroscopy does not have sufficient sensitivity to detect it at the levels present in the flow reactor.

2.2.2 Laser-Induced-Fluorescence RF Discharge Source

Another possible method to produce the A'-state is by N-atom recombination. The calculations of Partridge et al.[31] show that recombination of N-atoms on the $^5\Sigma$ potential is enhanced at lower temperatures. We produced N-atoms with an RF discharge source in a supersonic nozzle. The cooling expected during the expansion was expected to enhance the A'-state formation. N-atom recombination occurs at the throat of the nozzle. We used laser-induced-fluorescence (LIF) on the HIR bands to probe for the presence of $N_2(A')$ in the gas beam downstream of the nozzle. The following sections contain a description of the RF discharge source and the modifications necessary to incorporate the source in our existing vacuum chamber.

The RF discharge source was based on the design of Lee and coworkers.[45] He developed a high pressure, RF discharge nozzle beam source capable of producing a very intense ($\geq 10^{18}$ atoms sr^{-1} s^{-1}) supersonic beam of oxygen atoms. Two important developments lead to the achievement of such an intense source. First, an efficient impedance matching scheme was devised for coupling the RF power to the oxygen-rare gas mixtures. Second, techniques were developed for

localizing the discharge directly behind the orifice of the nozzle. The second development is quite important since atoms will recombine quite efficiently inthe slow gas flow downstream of the actual discharge. Extension of the discharge to the nozzle throat prevents significant recombination from occuring prior to the expansion.

A cross-sectional view of the source, with an enlarged view of the nozzle tip, appears in Fig. 31. The nozzle tube is made of quartz. Lee tested two materials, quartz and alumina. These were chosen because of their relatively high melting points. Alumina tubes, however, were found to be unsatisfactory. They tended to crack when subjected to large thermal gradients and arcing occurred between the outer surface of the tube and the RF coil whenever the two came into physical contact. Therefore quartz was chosen as the nozzle material despite being more difficult to fabricate into a nozzle.

In Lee's final design it was found necessary to incorporate a water cooling jacket to prevent the quartz orifice at the tip from melting and enlarging during the expansion of the hot gas mixture. Quartz is a poor thermal conductor so it was important that the water coolant flow be as close to the orifice as possible. With the water jacket the orifice was found to be stable with respect to enlargement. It is necessary to use low electrical conductivity water as coolant to reduce excessive RF power loss to the water. Lee found an added benefit of the jacket was the elimination of arcing between the plasma tube and the RF coils.

In our system the RF power is supplied by an ENI Power Systems ACG5 plasma generator which can deliver a maximum output of 500W. Impedance matching is accomplished by an Nye Viking MB-IV-A impedance matching network. Impedance matching is necessary since the effective plasma impedance, which varies as a function of plasma condition, is much larger than the 50Ω output impedance of the electronics. A schematic of the RF discharge circuit is given in Fig. 32.

—10 cm—
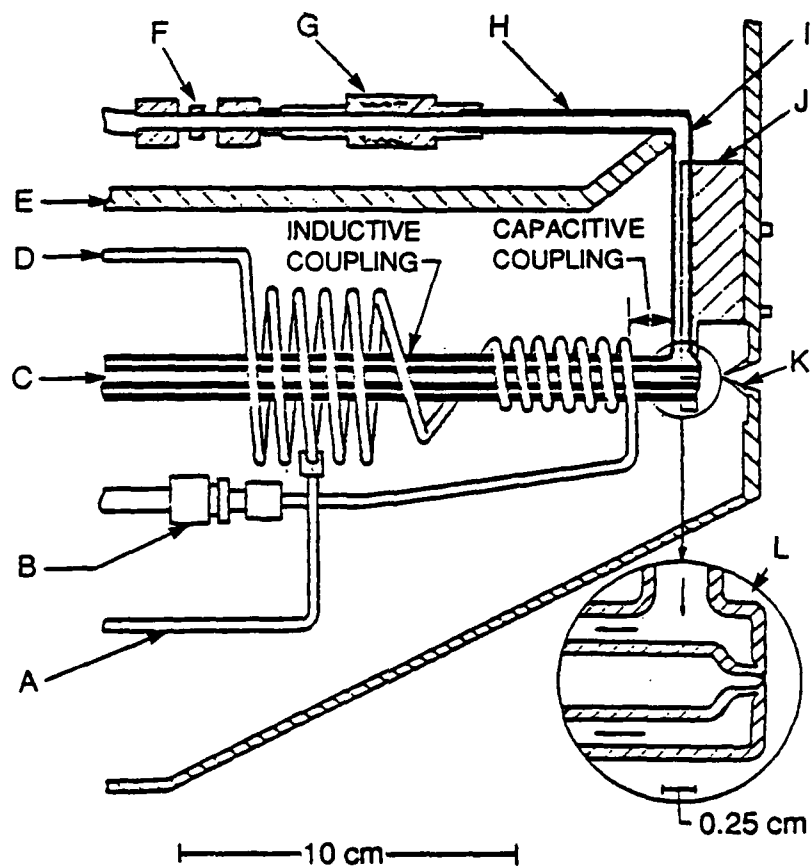
B-0431

a.   Variable ground tap
b.   Swagelock reducer
c.   Water-cooled quartz nozzle
d.   Coupling coil
e.   Quartz support rod for water inlet/output assembly
f.   Swagelock union joining copper and polyflo tubing
g.   Cajon VCO fitting
h.   Kovarpyrex section
i.   Graded seal, Pyrex to Vycor
j.   Aluminum support block to electrical ground
k.   Boron nitride skimmer, 0.88 mm
l.   4x enlargement of nozzle tip

Figure 31. Sectioned view of the internal source components (arrows
            indicate low conductivity water flow direction. (Ref. 46))

```
┌──────────────┐          ┌──────────────┐
│  ENI ACG5    │          │  IMPEDANCE   │
│   PLASMA     │          │  MATCHING    │
│  GENERATOR   │          │   NETWORK    │
└──────────────┘          └──────────────┘

  13.56 MHz                 13.56 MHz
  0-500 W                   0-650 W
  50 Ω OUTPUT               50 Ω INTPUT         AIR GAP
  SWR METER                 10-1000Ω OUTPUT     CAPACITOR
  MISMATCH PROTECTED        SWR METER           0-75 pf

                          ┌──────────────┐
                          │    FLOW      │
                          │   SWITCH     │
                          └──────────────┘

                          ┌──────────────┐
        RF ON/OFF         │ NESLAB COOLER│    COOLING FOR
                          │    500 W     │    PLASMA TUBE
                          └──────────────┘    & COILS

                                                      8-0430
```
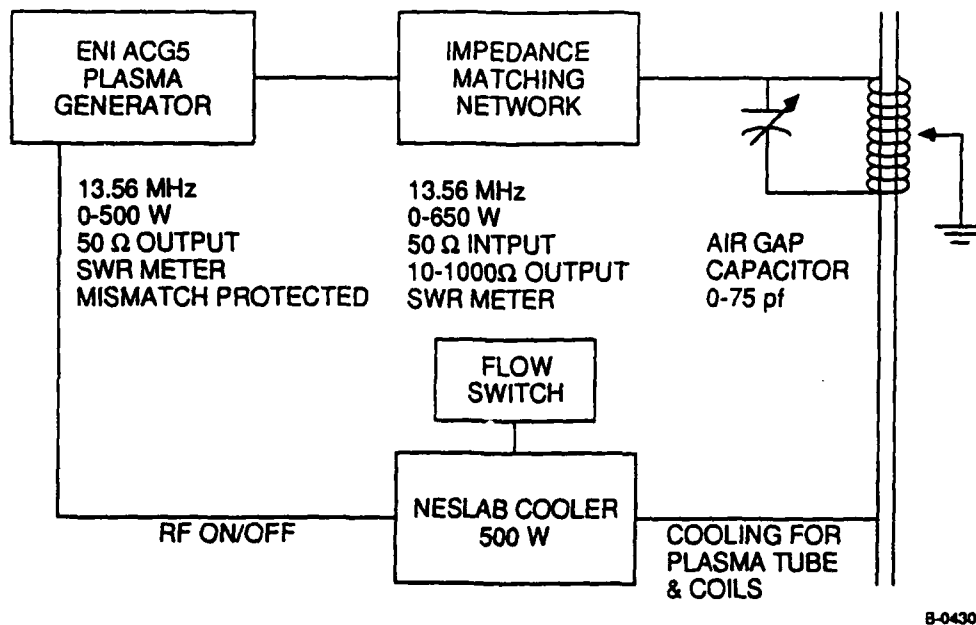
Figure 32.   Schematic of radio frequency source.

A variable ground tap on the tank coil is used to produce a large stepdown of the plasma impedance, as seen by the RF electronics, ideally to 50Ω. With this RF circuit it is possible to operate routinely at a standing wave ratio (SWR) of less than 1.05:1 for O_2/rare gas mixtures. For N_2 we found that the coupling was less efficient but that a SWR of less than 2:1 should be attainable.

To localize the plasma directly behind the nozzle orifice an electrically grounded block of aluminum (Fig. 31,J) is located around the nozzle tip. At high pressures coupling occurs between the front, small diameter tank coil turns and the aluminum block. As this coupling becomes stronger the plasma localizes towards the front of the discharge tube. The tank coil (Fig. 31,D) is differentially wound to further localize the plasma. The larger turns decouple from the plasma at higher pressures and increase the energy density of the localized plasma. It is important to note that the entire tank circuit, as shown in Fig. 32, is floated with respect to electrical ground. This is required if the RF coupling and the localization are to be effective.

49

Chamber Modifications

Our chamber used in the H_4^* experiments consisted of a 10 in. six-way cross with a smaller detection chamber attached at one end. Both chambers are pumped by a single diffusion pump. We modified the system to create two differentially pumped chambers. A stainless steel plate with a small hole was inserted between the two chambers and a second diffusion pump was added to the small detection chamber. A boron nitride skimmer was mounted on this plate on the large chamber side.

The RF discharge source is mounted on a 10 in. conflat flange which mounts on the large chamber directly opposite the detection chamber. Both RF and water vacuum feedthroughs to the discharge source have been made. Mounting brackets to hold the nozzle in place after alignment have also been made. Wherever possible non-metallic materials have been used to minimize coupling of the RF to mounting and support brackets.

Since we were using LIF detection, it was necessary to assemble Brewster angle windows with light baffles for the laser light to pass through. The photomultiplier (PMT) used to detect the LIF signal was equipped with a band-pass filter to isolate the HIR band transition of interest. However, the laser light is edge of the filter of the filter transmission curve wavelength of the quite close to the so scattered light must be carefully eliminated. A 1:1 imaging lens system was used to collect the fluorescence focus it on the PMT, and spatially define the collection region to minimize scattered light.

Unfortunately, our chamber is considerably smaller than Lee's, making for a very close fit. The proximity of the RF coils to the chamber walls allows the RF radiation to couple to the chamber instead of the discharge tube. Throughout our testing of the RF source we were unable to sustain a discharge at the nozzle tip. We therefore, replaced the nozzle assembly. The new nozzle had the RF discharge just outside the vacuum chamber. The nozzle extended into the chamber several inches but remained out of the detector field-of-view.

Laser-induced-fluorescence was used to probe for both HIR and the first positive bands of N_2. No signal was observed. The same experiment was also performed with the RF discharge replaced with a microwave cavity. Again no positive results were obtained. It was then decided to concentrate the remainder of the program on the DC discharge flow tube source where we were having some success.

2.2.3 Dishcarge Flow Reactor/LIF Studies

Our failure to observe the presence of any $N_2(A')$ using the optogalvanic detection system or the RF excited source prompted us to re-examine the use of LIF with a discharge flow reactor. Originally, we felt that the $N_2(A')$ molecule might be efficiently quenched in the gas phase. As a result of this assumption, we had sought to detect the A'-state within the discharge region (using optogalvanic spectroscopy) and in a collision-free molecular beam. The use of the discharge flow reactor allows us to better quantify the A'-state production role through observation of the HIR band emission. We are also able to produce and detect LIF over a larger collection volume in the flow reactor than in a molecular beam. Finally, simultaneous emission and LIF detection was possible in the discharge flow reactor. The results of this final set of experiments are outlined below.

Our approach to determining the collisional stability of the $A'^5\Sigma_g^+$ state of N_2 was as follows. We employed energy pooling of two $N_2(A^3\Sigma_u^+)$ molecules to pro-duce the $C''^5\Pi_g$ state. Radiative cascade through the C''-A' HIR bands results in production of the A'-state. The production rate can be determined absolutely via quantitative observation of the HIR band emission intensity. Laser-induced fluorescence (LIF) on the C''-A' transition is employed to probe for the presence of the A'-state. Calibration of the LIF detection system is accomplished approximately by comparison with LIF signals from the nearby $B^3\Pi_g-A^3\Sigma_u^+$ transi-tion. The $N_2(A^3\Sigma)$ population may be inferred from HIR band emission intensities using the HIR energy pooling rate coefficient or directly using $N_2(A-X)$ Vegard-Kaplan band emission intensities. A simple kinetic model, tied to absolute population measurements, is used to predict the A'-state population. The HIR band LIF intensities were compared with intensities predicted by the

calibrated computer model. The gas phase $N_2(A')$ lifetime required to explain the observed signal level was then determined from the model. The experiment is described in more detail below.

The discharge flow apparatus is shown schematically in Fig. 33. The apparatus consists of an $N_2(A^3\Sigma)$ generator, a short flow section, diagnostics section, and pumping facility. The flow section was provided to allow the $N_2(A')$ to build to maximum concentration, to reduce scattered light from the discharge, and to add various reagents. The diagnostics section provided for observation of passive emission and LIF at the same point in the flow reactor. Passive emission was detected using a 0.35m monochromator (McPherson 270) equipped with a cooled GaAs PMT (HTV R943-02) operated in photon counting mode. A rate meter on the photon counter (Pacific Photometrics) was interfaced to a laboratory computer for signal acquisition. The absolute sensitivity of the detection
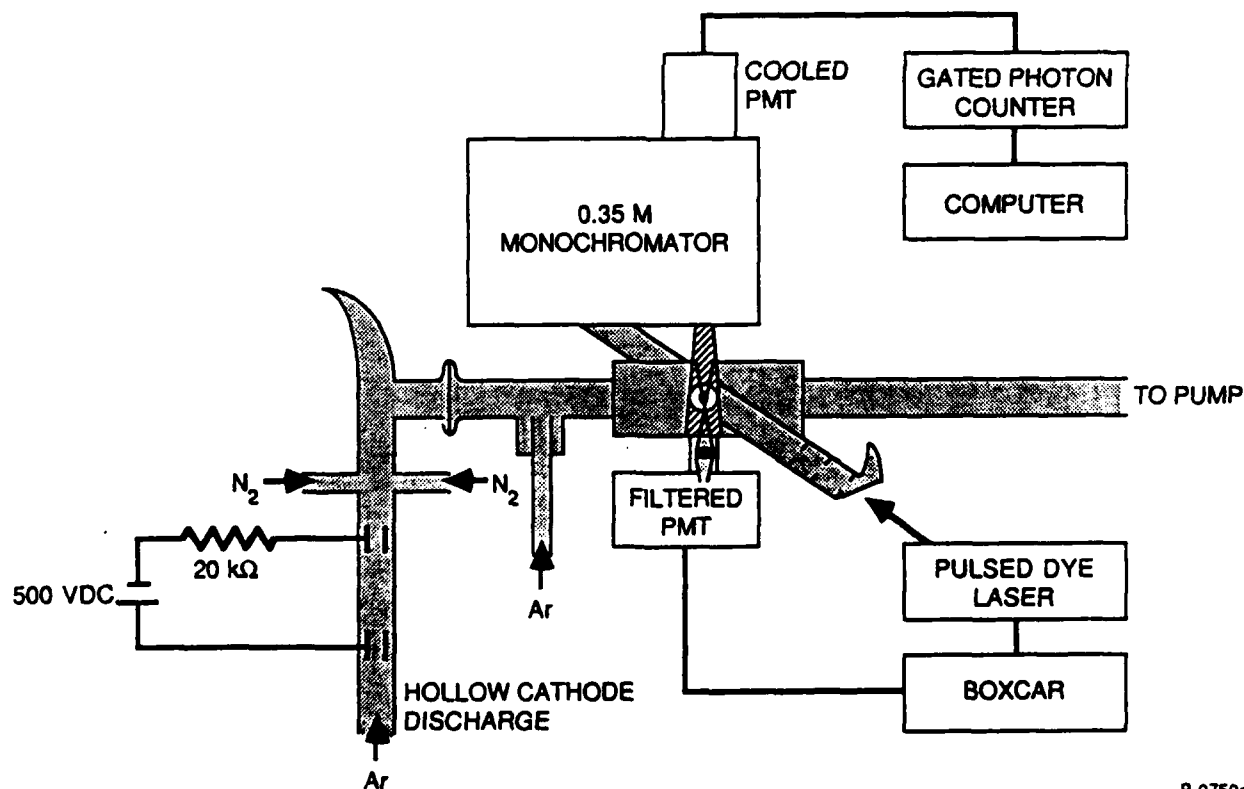
Figure 33. Schematic diagram of the discharge flow reactor and LIF detection system used in the experiments.

system was calibrated using the well known A/NO air afterglow in the 400 to 900 nm region.[40,46] The absolute calibration was extended to 200 nm by comparison with deuterium and quartz halogen irradiation standards.

A Nd:YAG pumped tunable dye laser (Quantel YG581C/TDL50) operating with LDS 698 dye was used to excite fluorescence from the N_2 A'-state and A-state in the diagnostics section. The section is internally blackened with a Teflon coating and equipped with long baffle arms to reduce scattered light. The LIF is detected with a baffled and filtered PMT (HTV R955). An f/2 lens was used to image fluorescence on to the PMT photocathode. The combination of a Schott RG-9 color filter and 750 nm long-pass interference filter, along with the PMT long-wavelength cut-off, limited the wavelength range of the detection system to 750 to 900 nm. Approximately 50 percent of the emission from N_2(B, v=3) and N_2(C", v=2), the levels pumped in the LIF detection experiments, occurs in this wavelength region. Signals from the PMT were fed to a high-speed current amplifier (Ithaco 1211) and then to a boxcar signal averager. The LIF signals were recorded with a laboratory computer and corrected for variations in laser intensity.

The $N_2(A^3\Sigma)$ used in this study was produced by energy transfer from metastable $Ar(^3P_{0,2})$ to N_2. This technique has been described extensively in the literature.[47,48] The metastable Ar was produced by passing Ar though a low power DC discharge (500 VDC, 2 mA) at a flow rate of approximately 4000 μmole s^{-1}. Small flows of N_2 (10 to 250 μmole s^{-1}) were added downstream of the discharge. In some experiments a 5 percent Ar in He mixture was passed through the discharge in order to use He as the buffer gas. A small flow of O_2 could be injected downstream of the $N_2(A^3\Sigma)$ generator in order to quench the N_2(A). This was done occasionally in order to eliminate all chemiluminescence and check for the presence of scattered light from the discharge. In all cases flows were measured using calibrated mass flow meters. Cell pressures were measured using a calibrated capacitance manometer. All reagent gases were UHP (99.999) and were used without further purification. The flow reactor was pumped by two 17 cfm and one 27 cm mechanical vacuum pumps connected in a parallel manifold. In this configuration flow velocities in excess of 3700 cm s^{-1} at pressures of 2 Torr were attainable.

2.2.4 Results

Initial experiments were conducted using Ar as a buffer gas at pressures of approximately 4 Torr. Observation of N_2 HIR emission showed that the intensity was maximized under these conditions at N_2 mole fractions of approximately 0.05. An emission spectrum of the region from 610 to 820 nm, recorded at a point 5 ms downstream of the $N_2(A)$ generator, is shown in Fig. 34. The spectrum includes the data and a fit to the data indicating the presence of both the N_2 (C"-A') HIR bands and the $N_2(B-A)$ First Positive bands. The transition probabilities calculated by Partridge et al.[36] were used in calculating the fitted spectrum. It is evident that these parameters do quite a good job of reproducing the experimental spectrum. The spectrum of the C"-A' transition is dominated by emission from vibrational levels 2 and 3. Previous studies by Piper[40] showed that these levels are produced nearly exclusively by the energy pooling reactions involving combinations of $N_2(A, v=0)$ and $N_2(A, v=1)$
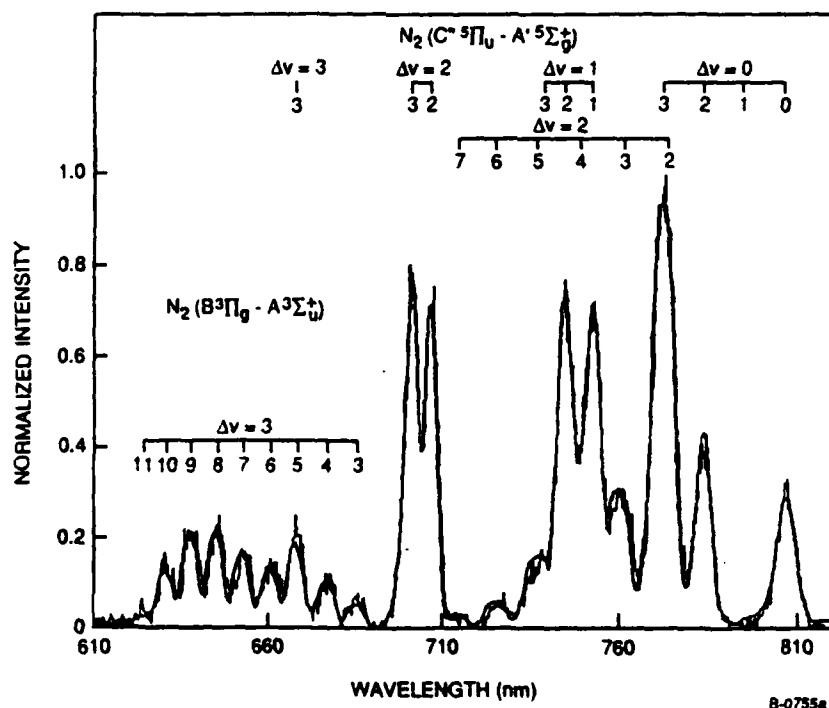
Figure 34. Visible emission spectrum of N_2 resulting from the $N_2(A)$ energy pooling reaction. The important C"-A' and B-A transitions are indicated.

A lower limit on the $N_2(A')$ production rate is given by the $C''-A'$ emission intensity. This emission intensity can also be used to determine the $N_2(A)$ concentration at that point in the flow reactor. The total $N_2(A')$ concentration at any point in the flow reactor is the integral of $N_2(A')$ production and loss processes from the $N_2(A)$ generator to that location. Initially, we assume that only quenching at the walls of the flow reactor is responsible for the loss of $N_2(A')$. The production and loss of $N_2(A)$ and $N_2(A')$ can be described approximately by the set of reactions:

$$N_2(A) + N_2(A) \rightarrow N_2(C'') + N_2(X) \tag{27}$$

$$N_2(A) + N_2(A) \rightarrow N_2(B,C) + N_2(X) \tag{28}$$

$$N_2(A) + wall \rightarrow N_2(X) \tag{29}$$

$$N_2(C'') \rightarrow N_2(A') + h\nu(HIR) \tag{30}$$

$$N_2(A') + wall \rightarrow N_2(X) \quad . \tag{31}$$
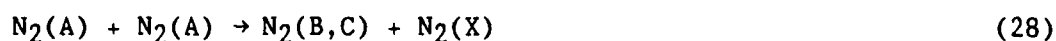
Other collisional and non-collisional pathways for deactivation of $N_2(A')$ can be described by inclusion of an additional pseudo first-order loss term:

$$N_2(A') \rightarrow products \tag{32}$$

The radiative rate of the C''-state is sufficiently large so that the C''-state concentration may be considered to be in steady state in the field of view of the detection system. Hence, the rate of Eq. (27) can be set equal to the rate of Eq. (30):

$$k_1[N_2(A)]^2 = k_4[N_2(C')] = I_{HIR} \tag{33}$$

where I_{HIR} is simply the total Herman Infrared Band volume emission rate. Thus, the $N_2(A)$ concentration may be determined from the HIR band absolute emission rate:

$$[N_2(A)] = \{I(HIR)/k_1\}^{1/2} \quad . \tag{34}$$

The energy pooling rate coefficients for the formation of the $N_2(C'')$ state have been measured by Piper.[40] The rate coefficients and the vibrational levels of the C"-state that are excited depend on the degree of vibrational excitation present in the $N_2(A)$. Under our experimental conditions the $N_2(A)$ is produced primarily in v=0. Hence, we have used Piper's rate coefficient for pooling of two $N_2(A, v=0)$ molecules, $8.1 \pm 2.3 \times 10^{-11}$ cm^3 $molecule^{-1}$ s^{-1}, in determining the $N_2(A)$ number density. Thus, under typical experimental conditions the HIR band emission measurement gives an $N_2(A)$ number density of 9×10^9 molecules cm^{-3} 5 ms downstream of the generator.

This estimate of the $N_2(A)$ number density is confirmed by direct observation of the $N_2(A-X)$ Vegard-Kaplan Bands. Figure 35 shows a spectrum of the region from 200 to 400 nm. The fit to the spectrum clearly identifies features from $N_2(A, v=0,1)$ and $N_2(C, v=0-3)$. The $N_2(C)$ emission is produced from the $N_2(A)$ energy pooling reaction. The emission from the NO(A-X) transition evident in

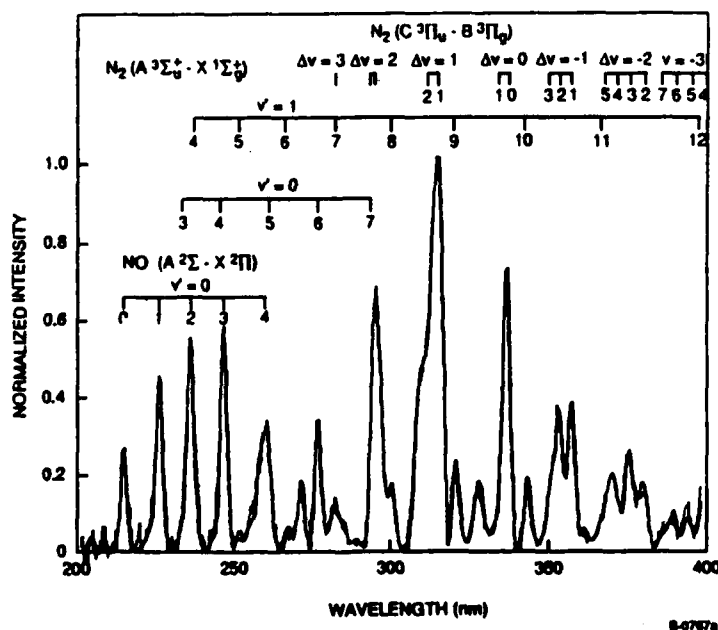Figure 35. UV emission spectrum of N_2 from $N_2(A)$ energy pooling. Features of the A-X and C-B transitions are indicated. Also present are features from the NO(A-X) and OH(A-X) transitions resulting from the presence of low-level impurities.

the spectrum is due to excitation of small amounts of discharge-produced NO by $N_2(A)$. Also present, but not identified in the spectrum, is emission from the OH(A-X) transition which is also due to a low-level impurity. The direct determination of $N_2(A)$ concentrations from the A-X band intensities in general indicated $N_2(A)$ concentrations consistent with HIR emission intensity determinations.

The decay of $N_2(A)$ in the flow reactor can be modeled to determine the initial $N_2(A)$ concentration at the exit of the generator. This concentration must be determined in order to calculate the total $N_2(A')$ production up to the observation point. The decay of $N_2(A)$ is given by the expression:

$$\frac{d[N_2(A)]}{dt} = (k_1+k_2)[N_2(A)]^2 - k_3[N_2(A)] \qquad (35)$$

where the factor of two usually found in the rate expression reflecting the loss of two $N_2(A)$ molecules per pooling event has been excluded. This is done to account for the fact that, under most experimental conditions, one $N_2(A)$ molecule is regenerated from the pooling reaction via radiative cascade through the $C^3\Pi_u$ and $B^3\Pi_g$ states. The rate coefficient for wall loss in a diffusion dominated regime, k_3, is given by:[49]

$$k_3 = 3.66 \; D/a^2 \qquad (36)$$

where D is the diffusion coefficient of $N_2(A)$ in the buffer gas and a is the tube radius. The diffusion coefficient can be calculated approximately from kinetic theory[50] to be 160 $cm^2 \; s^{-1}$ at a pressure of 1 Torr and scales inversely with pressure. Under our conditions k_3 typically has a value of 80 s^{-1}. The value of k_2, the energy pooling rate coefficient for production of all products other than the C"-state, is estimated by Piper[40] to be approximately 3×10^{-10} cm^3 molecule^{-1} s^{-1}. Thus, it is clear that at these $N_2(A)$ concentrations wall loss is primarily responsible for the loss of $N_2(A)$. Equation (36) can be solved analytically by neglecting pooling or exactly using a simple numerical model to yield the $N_2(A)$ concentration at the generator exit port.

The equation governing the production and loss of $N_2(A')$ is given by:

$$\frac{d[N_2(A')]}{dt} = k_4[N_2(C'')] - \{k_5 + k_6\}[N_2(A')] \tag{37}$$

where the value of k_5, wall loss rate coefficient for the A'-state, is assumed to be the same as for the $N_2(A)$ state and $k_4[N_2(C'')]$ is shown in Eq. (33) to be the total HIR band emission intensity. By substitution of Eq. (33) into Eq. (37) one can relate the expected A'-state concentration to the $N_2(A)$ concentration:

$$\frac{d[N_2(A')]}{dt} = k_1[N_2(A)]^2 - \{k_5 + k_6\}[N_2(A')] \quad . \tag{38}$$

Given the initial $N_2(A)$ concentration determined from Eq. (36) the concentration of $N_2(A')$ can be calculated at any point in the flow reactor using a simple numerical model. It was initially assumed that other loss processes were negligible ($k_6 = 0$). The model predicted that $N_2(A')$ concentrations on the order of 4×10^7 molecules cm^{-3} could be expected in the observation region, 5 ms downstream of the injector.

Approximate calibration of the LIF detection system was accomplished by observing the LIF produced by pumping the $N_2(B^3\Pi_g-A^3\Sigma_u^+, 3-0)$ band. The origin of the band is at 685.83 nm. This is a spectral region where no absorption is expected from the $N_2(C''-A')$ transition. A typical spectrum of LIF from the 3-0 band is shown in Fig. 36. The transition is a $^3\Pi$(Case a)-$^3\Sigma$ transition with 27 possible branches. Several of the main branches and satellite branches are indicated in the figure. The signal intensity at the P_{11} branch head was chosen for determining the detection sensitivity. The absolute $N_2(A^3\Sigma, v=0)$ concentration was determined by the techniques described above.

Several issues must be considered in using this method to determine the sensitivity of the LIF technique for detecting the A'-state. The primary issue
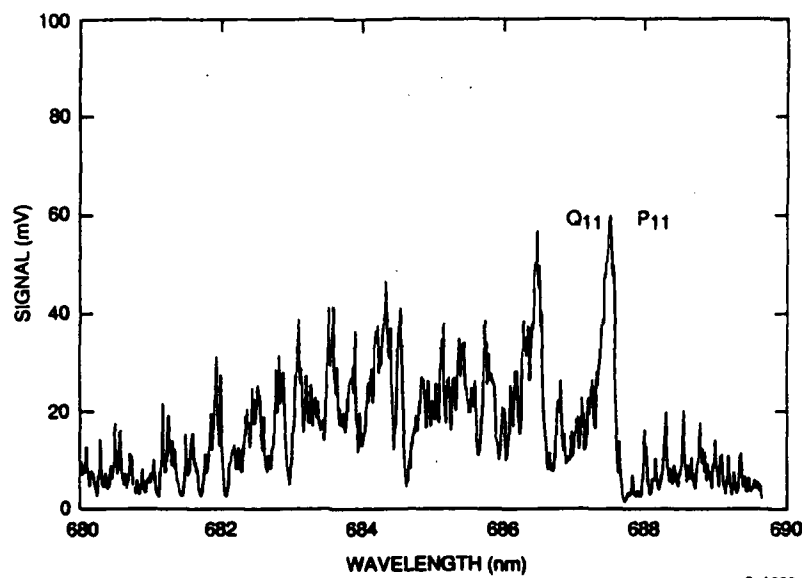
Figure 36. LIF excitation spectrum of the $B^3\Pi_g-A^3\Sigma_u^+$ 3,0 band transition observed in the discharge flow reactor. The Q_{11} and P_{11} branch band heads are indicated in the figure.

is the actual oscillator strength of the C"-A' transition relative to the B-A transition. As mentioned in the introduction, the calculated radiative lifetime for the C"-A' transition, 4.3 µs, conflicts with some of the data on quenching of C"-state emission. The quenching data suggests that the lifetime of the C"-state is closer to 40 ns. This lifetime would imply a much stronger absorption oscillator strength for the transition. The discrepancy will be addressed further in the discussion session; however, the primary effect of an increased oscillator strength for the C"-A' transition would be a lowering of the detection limit for the A'-state by approximately a factor of one hundred. Thus, our measurements would give a result which is an upper limit on the A'-state concentration and hence a lower bound on the effective loss rate.

An LIF spectrum of the region from 700 to 710 nm is shown in Fig. 37. The 2-0 and 3-1 bands of the C"-A' transition should be excited in this wavelength region. Though absorption features are observed in this region, they can be assigned to the N_2(B-A, 8-6) transition. This assignment is confirmed by

59
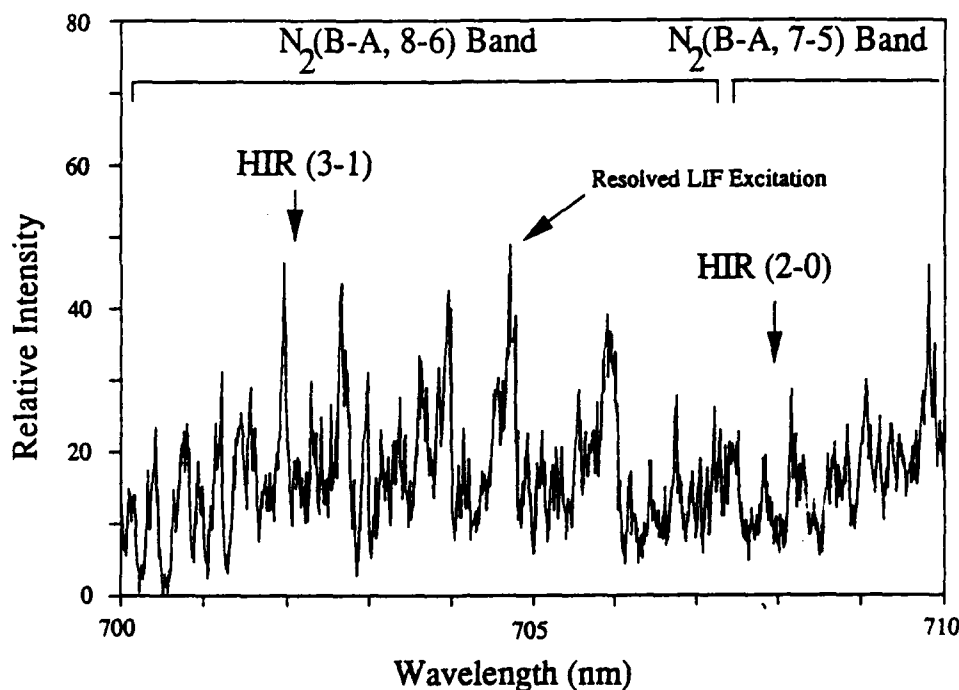
Figure 37. LIF excitation spectrum for the region from 700 to 710 nm. Features of the B-A, 8,6 and 7,5 transition are identified. Arrows show the expected location of the HIR 3,1 and 2,0 bands. The excitation point for the spectrum of Fig. 38 is shown.

resolving the fluorescence excited by the laser. A typical resolved emission spectrum is shown in Fig. 38. The only discernible emission features are due to transitions originating from $v=8$ and $v=7$ of the B-state. Population of N_2 (B, $v=7$) is due to vibrational relaxation of B, $v=8$ by the Ar buffer. Thus, no emission from the $N_2(C"-A')$ system is excited by the laser within the detection limits of the system. The detection sensitivity used in the LIF spectrum of the 700 to 710 nm region is a factor of 1000 better than than the sensitivity used in recording the spectrum of the $N_2(B-A, 3-0)$ band. Observation of the poorly populated and weakly absorbing $v=6$ level of the A-state illustrates the detection limits of the system. Comparison of the noise levels observed in this spectrum with the signal levels obta d in the spectrum of Fig. 37, corrected for the differences in the absorption strengths for the B-A, 3-0 and $C"-A'$, 2-0 bands, establishes a detection sensitivity of approximately 1×10^6 molecules cm^{-3}.
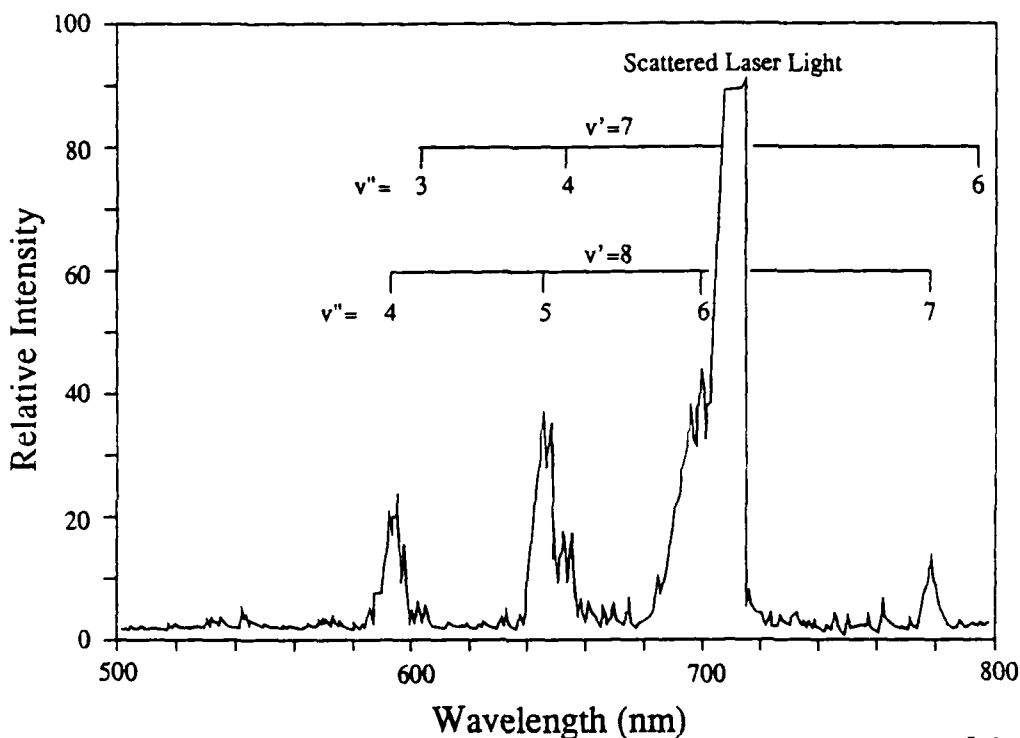
8-1213

Figure 38.   Resolved LIF spectrum for one of the absorption bands of Fig. 37.
The features present can all be identified as originating from the
B-A transition.   Excitation of the 8,6 band is clearly indicated.
Emission from B, v=7 is probably due to vibration relaxation of the
B-state.

The simple numerical model used to predict the expected $N_2(A')$ densities at the
observation point in the discharge flow reactor can be used to determine a
lower limit on the loss rate (k_6) for $N_2(A')$ consistent with a concentration at
our detection limit.   The traces in Fig. 39 show the expected temporal profile
for $N_2(A')$ when only wall loss (Trace a) and a loss rate of 3200 s^{-1} (Trace b)
is included in the model.   When the loss rate of 3200 s^{-1} is incorporated in
the model an $N_2(A')$ concentration equivalent to the estimated detection limit
is predicted at the detection point.   Hence, we can place an upper limit on the
A'-state lifetime of approximately 0.3 ms.   In our experiments we explored a
range of N_2/Ar mixture ratios (1 to 20 percent N_2), discharge conditions (300
to 600 VDC), and pressures (2 to 5 Torr).   In addition, we passed N_2/Ar and
N_2/Ar/He mixtures directly through the DC discharge.   This method of production
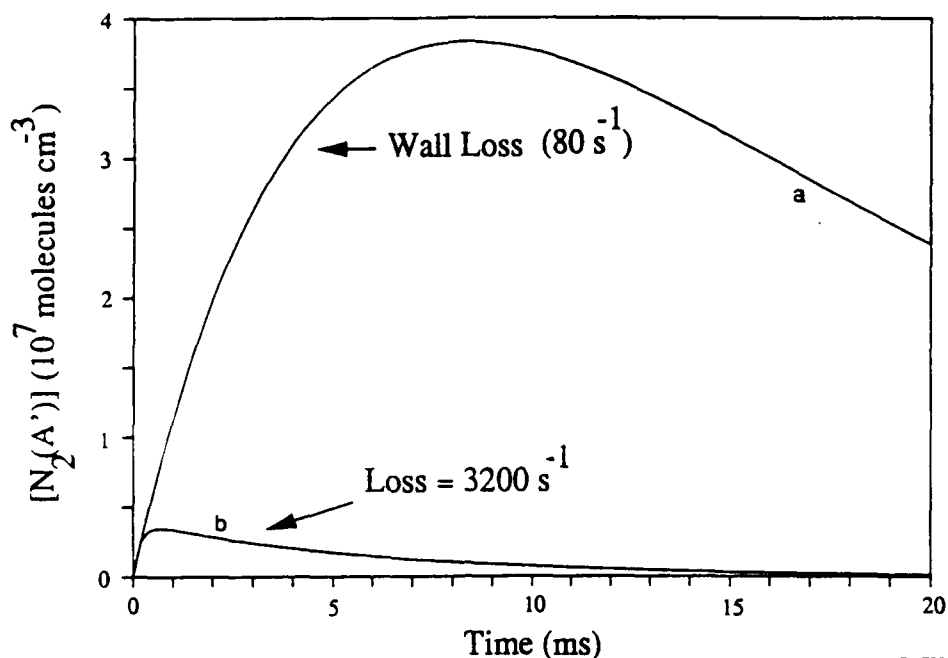
Figure 39. Model predictions for the temporal evolution of the $N_2(A')$ population in the discharge flow reactor. Trace a shows the behavior expected if wall loss was the only mechanism responsible for quenching of the A'-state. Trace b shows the behavior expected for a loss rate of 3200 s^{-1}. This rate produces a concentration of A' at our detection limits.

enhances the observed $N_2(C''-A')$ emission intensity at the expense of producing N-atoms and perhaps other metastable states of N_2. In addition, He/Ar mixtures were co-discharged and N_2 added downstream. Under no set of conditions was LIF on the C''-A' transition observed.

2.2.5 Discussion

We have conducted a series of experiments to determine the gas-phase lifetime of the A'-state of N_2. Though the LIF calibration method employed in the study was not precise, the experiments do infer a lifetime for the $^5\Sigma$ state which is much shorter than expected for a spin-forbidden decay process. Our experiments do not provide any direct evidence for any of the possible decay mechanisms. However, some indirect evidence provides support for a collisional decay channel through the $B^3\Pi_g$ state.

An expanded potential energy diagram for the A'-state and near isoenergetic levels of the $B^3\Pi$ and $A^3\Sigma$ state is shown in Fig. 40. The diagram shows that the lowest vibrational level of the A'-state is near-resonant with v=10 of the $B^3\Pi_g$ state. Also, the barrier to predissociation for the A'-state occurs at v'=13 of the B-state. The latter observation provides evidence for invoking curve crossing to the A'-state as the mechanism for predissociation of the B-state. Thus both collisional and spin-orbit coupling to the B-state might be evident in the spectrum of levels 10-12. A recent study of the high-resolution LIF spectrum from the $N_2(B^3\Pi_g-A^3\Sigma_u^+$, 10-6) transition revealed no apparent perturbations in the rotational levels of the B-state.[51] In addition, no other studies have reported any perturbations in the spectra of levels 10-12.[52] Thus, there appears to be no direct evidence from the spectroscopy of the B-state to indicate spin-orbit coupling to the A'-state.
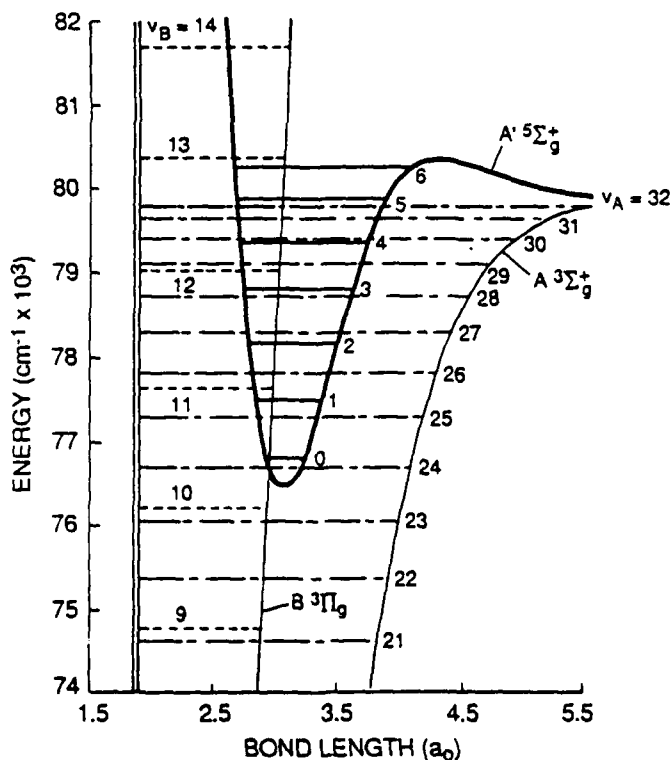
B-0751a

Figure 40. Expanded energy level diagram of the A'state redrawn from the results of Partridge et al.[36] The figure illustrates the potential for coupling of the A' and B states.

The evidence for collisional coupling of the B-state to the A'-state come from measurements of the energy pooling rate coefficient to form the B-state. If the energy pooling reaction is studied using an Ar buffer gas much of the information on the distribution of vibrational levels populated in the B-state is washed-out by rapid vibrational relaxation. If He is employed as a buffer gas vibrational relaxation is less efficient and much of the nascent vibrational distribution is preserved in the emission spectrum. A typical spectrum of emission from the energy pooling reaction from 560 to 720 nm using He as a buffer gas is shown in Fig. 41. In contrast to the spectrum of Fig. 38, a strong enhancement in the population of v=10 of the B-state is observed. This enhancement has been previously observed.[53] Thus, it would appear that collisional coupling from the A'-state to the B-state may be a mechanism for the decay of the A'-state.
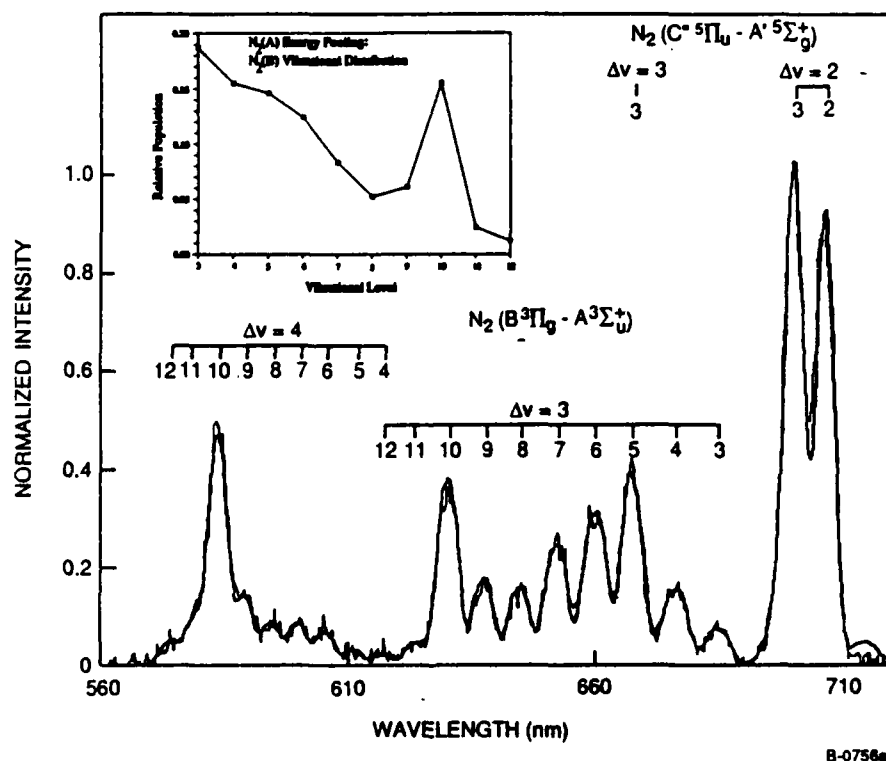

B-0756a

Figure 41. Visible emission spectrum of N_2 due to $N_2(A)$ energy pooling in a dominantly He buffer gas. The enhancement of the population of v=10 of the B-state is indicated in the inset plot of the vibrational distribution.

Additional evidence for the coupling comes from the magnitude of the rate coefficients to form the B-state and the C"-state from the energy pooling reaction. The energy pooling rate coefficient for the direct production of $N_2(B)$ from two $N_2(A, v=0)$ molecules, as measured by Piper,[53] is $7.7 \pm 1.1 \times 10^{-11}$ cm^3 molecule^{-1} s^{-1}. This rate coefficient can be compared with his measurement for the formation of the C"-state, $8.1 \pm 2.3 \times 10^{-11}$ cm^3 molecule^{-1} s^{-1}. Thus, it is possible that a significant fraction of the direct production of B-state is actually derived from production of the C"-state followed by radiative cascade to the A'-state and collisional coupling to the higher B-state vibrational levels. However, some direct production of the B-state must occur. Piper's observation that energy pooling of vibrationally excited $N_2(A)$ favors production of lower B-state levels is not consistent with the cascade mechanism. In addition, pooling of $N_2(A, v=0)$ molecules also shows enhanced production of B, v=2.

The upper limit on the stability of the A'-state is uncertain, to a large degree, due to the apparent discrepancy in the lifetime of the C"-state. Predissociation of the C"-state can be excluded as the cause for the apparent reduced lifetime. The energy pooling rate coefficient would have to be significantly larger than gas kinetic in order to produce a C"-state population for which the predissociation rate was 100 times greater than the fluorescence rate. Similarly, direct coupling of the C and C" states is unlikely. At the pressures employed in most of the experiments which have investigated this system radiative decay of the C-state should be much more efficient than collisional energy transfer. Further investigation of this problem is warranted.

Our experiments in which we vary the N_2 concentration indicate that N_2 is not primarily responsible for coupling of the two manifolds. At the lowest N_2 concentrations employed a gas-kinetic coupling rate coefficient would be required to couple the levels and significant variations in the B-state, v=10 enhancement would have been observed. It would appear more likely that Ar or He, which are both present in much greater concentrations, may be responsible for the coupling. The production of $N_2(A')$ in either a supersonic jet or in a

rare gas matrix may reduce the collisional coupling to the B-state and enable a more rigorous determination of the lifetime of this state.

2.2.6 Conclusions

We have observed production of the $A'^5\Sigma_g^+$ state of N_2 from the energy pooling of $N_2(A^3\Sigma_u^+)$ molecules. Laser-induced fluorescence on the $C''^5\Pi_u-A'^5\Sigma_g^+$ transition failed to detect the presence of A'-state molecules. Based on simple kinetic arguments, we have been able to place an upper limit on the lifetime of the A'-state under our experimental conditions of 0.3 ms. Observation of enhanced emission from v=10 of the $B^3\Pi_g$ state suggests that collisional coupling of the A' to the B-state is responsible for the decay of this state.

The production and storage of the A'-state under cryogenic conditions via matrix isolation may enhance its stability. The energy gap between v=10 of the $B^3\Pi_g$ state and v=0 of the $A'^5\Sigma_g^+$ state is approximately 650 cm^{-1} which is much smaller than kT at 4K. Thus collisional coupling at this temperature should be quite inefficient. In addition, the magnitude of spin-orbit coupling to adjacent electronic states is also reduced at low temperatures. The selection rules for spin-orbit coupling to adjacent electronic states is also reduced at low temperatures. The selection rules for spin-orbit coupling require that total angular momentum be conserved ($\Delta J=0$) and that spin and orbital angular momentum have the selection rules (Reference 54):

$$\Delta L = 0, \pm 1 \qquad \Delta S = 0, \pm 1 \; . \qquad (39)$$

The total angular momentum, J, is the sum of the spin, orbital, and rotational contributions (neglecting nuclear spin). At cryogenic temperatures (and in the matrix) rotational motion is frozen into the lowest rotational state and rotational transitions are not possible. Hence, the spin-orbit coupling selection rules require that $\Delta S = \Delta L$. Since there are no other nearby quintet states, spin-orbit coupling of the $^5\Sigma$-state requires $\Delta S = \pm 1$. Hence, the $^5\Sigma$ state can only couple to $^7\Pi$ or $^3\Pi$ states. Thus, the $B^3\Pi_g$ state is the only state which is allowed couple to the $A'^5\Sigma_g^+$ state. The reduced degree of

rotational motion imposed by the matrix results in a reduced number of pathways for spin-orbit interaction and hence promotes the stability of the $^5\Sigma$ state.

Thus, the challenge to the further stabilization of the $A'^5\Sigma$ state is to form and stabilize this molecule in a cryogenic matrix. In the paragraphs below we discuss the previous work on cryogenic trapping of excited N_2 and the evidence which suggests that the A'-state can be matrix stabilized in a form useful for propulsion.

The concept of energy storage by cryogenic trapping of energetic radical and excited state species in matricies arose some 30 years ago and was vigorously pursued in an intense research program at the National Bureau of Standards (now NIST).[55,56] The program focussed on the trapping of ground state atomic and molecular radical species. However, in the course of the research, several investigators observed complex fluorescence/phosphorescence effects which were ascribed to cryogenic trapping and subsequent energy transfer involving excited state species. Much of this early work can be found in the papers of Broida and coworkers (Refs. 57-60 and citations therein) and Brocklehurst & Pimentel.[61] In brief, these investigators introduced flowing discharged N_2/rare gas mixtures into a liquid He cooled trap where the discharged species were condensed. Upon cessation of the discharge, the condensed samples were observed to glow in the visible, with characteristic decay times on the order of seconds to minutes, indicating rather lengthy storage of the trapped electronic energy. The solid afterglow was also observed to follow a rather complex temperature dependence upon warming the sample from 4.2 K to 35 K, indicating that the energy decay pathways were a function of matrix material and matrix diffusion times.

More recently, the excitation of emissions in N_2 at cryogenic temperatures was summarized and further addressed by Dressler and coworkers.[62-64] They showed that these emissions were, for the most part, independent of the excitation source employed. Furthermore, they were all related to the presence of the excited ^2D and ^2P states of nitrogen atoms. The band systems observed can be assigned to the following processes: a) phonon assisted emission on the ^2D-^4S and ^2P-^2D transitions with characteristic lifetimes of 37s and approximatly 1ms

respectively, b) a Stokes-shifted transition corresponding to emission on the $^2D-^4S$ transition coupled to excitation of a 2300 cm^{-1} vibron mode in the N_2 crystal lattice, and c) Stokes and anti-Stokes sequence band emission corresponding to the formation and radiation of $N(^2P)$ and $N(^2D)$ coupled with high vibrational transitions in the N_2 lattice. These features are summarized in Fig. 42 for both the $^2D-^4S$ and $^2P-^2D$ transitions.

The appearence of these vibrational satellites has been ascribed to the quenching of matrix created $N_2(A^3\Sigma_u^+)$ by N-atoms to produce either $N(^2D)$ or $N(^2P)$, with the remaining energy taken up in the vibrational modes of the matrix. Vibron levels as high v=14 may be excited in the formation of $N(^2D)$ and v=8 in the formation of $N(^2P)$. These limits are consistent with the cut-off in vibrational levels observed corresponding to excitation of the respective states. Emission from the $N_2(A-X)$ Vegard-Kaplan bands was readily observed by Vegard in excited N_2-doped solid rare gases,[65] but was observed to weaken if the matrix was irradiated with electrons. It was hypothesized that the gradual
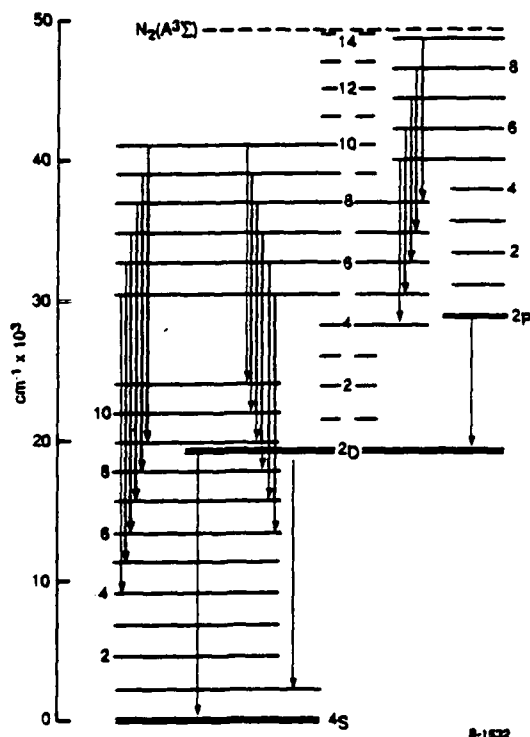

Figure 42. Energy level diagram and transitions, of the visible and near-infrared luminescence of N-atom-doped solid N_2.

increase in N-atom density accompanying the irradiation resulted in the well-known quenching of $N_2(A)$ by N_2.[66-68] Thus, the lifetime of the excited triplet appears to be directly related to the N-atom density in the matrix.

The lifetimes reported for $N(^2D)$ and $N(^2P)$ in solid N_2 represent a reduction of ~10^3 and ~10^4 over the respective gas-phase lifetimes.[69] Dressler and coworkers attribute the lifetime shortening to a matrix-induced increase in the transition rate. However, no evidence would appear to support this interpretation over a collisional matrix relaxation process. This distinction is critical since radiation trapping can be used to retain stored energy in a thick matrix if an increase in transition rate is responsible for the shortened lifetimes. Otherwise, this excitation is lost to the matrix heat bath.

The lifetime of the $N(^2D-^4S)$ transition and the $N_2(A-X)$ bands as a function of matrix material and temperature were studied by Tinti and Robinson.[70] The lifetime of the $^2D-^4S$ transition appeared to lengthen as the rare gas matrix partner became lighter. Lifetimes of 340 s, 18 s, and 7 s were measured for Ne, Ar, and Kr matricies respectively. The lifetime of $N_2(A, v=0)$ showed similar lengthening with rare gas partner. However, unlike the N-atom transitions, the $N_2(A-X)$ transition lifetime was nearly identical to the reported gas phase lifetime, within the uncertainties of the respective measurements. This can be attributed to the reduced probability of spin-orbit coupling between the molecule and the host matrix. This is an extremely important observation. The magnitude of the matrix elements which control these couplings are directly related the the viability of the $N_2(A'^5\Sigma_g^+)$ state as an energy storage medium. The data of Tinti and Robinson also show that the lifetime is independent of N_2 dosing levels up to 1 percent. No data was reported for higher dosing levels. The data also agrees well with the calculations of Happer and coworkers[71] who showed that the lifetime of pure spin-polarized N_2 crystals is quite short due to the magnetic dipole-dipole interactions in the crystal. However, they also noted that the stability of high-spin states may be enhanced by dilution in a diamagnetic matrix like solid hydrogen. Both theory and experiment point to the dilution in a light atom matrix as a means of stabilizing these high spin systems. Therefore, we believe that this system merits further investigation.

3. REFERENCES

1. Rubenstein, M. and Shavitt, I., "Theoretical Study of the Potential Surafce for the H_4 System by Double Zeta Configuration Interaction Calculations," J. Chem. Phys. <u>51</u>, 2014 (1969).

2. Wilson, C.W., Jr. and Goddard, W.A., III, "Ab Initio Calculations on the $H_2 + D_2 = 2HD$ Four Center Exchange Reaction I: Elements of the Reaction Surface," Chem. Phys. <u>51</u>, 716 (1969).

3. Wright, J.S., Can. J. Chem. <u>53</u>, 549 (1975).

4. Goddard, J.D. and Csizmadia, I.G., "A Note on SCF MO CI Calculations on the Ground and Low-Lying Excited States of Rectangular H_4: An Excimer Model System," Chem. Phys. Lett. <u>43</u>, 73 (1976).

5. Nicholaider, C.A., and Zdetsis, A., "Theory of Chemical Reactions of Vibrorically Excited $H_2(B^1\Sigma_u^+)$. II. Noble Gas Dihydrides," J. Chem. Phys. <u>80</u>, 1900 (1984).

6. Nicholaides, C.A., Petsalakis, I.D., and Theodorakonoulos, G., "Theory of Chemical Reactions of Vibronically Excited $H_2(B\text{-}\Sigma_u^+)$. I. Prediction of a Strongly Bound Excited State of H_4," J. Chem. Phys. <u>80</u>, 1705 (1984).

7. Nicholaides, C.A., Petsalakis, I.D., and Theodorakopoulos, G., "Theory of Chemical Reactions of Vibronically Excited $H_2(B^1\Sigma_u^+)$. III. Formation of Bound Excited States of the $(H_2)_2$, $(H_2)_3$, and $(H_2)_5$ Clusters," J. Chem. Phys. <u>81</u>, 748 (1970).

8. Fink, E.H., Akins, D.L., and Moore, C.B., "Energy Transfer in Monochromatically-Excited Hydrogen $((B^1\Sigma_u^+)$. I. Excitation Processes, Electronic Quenching, and Vibrational Energy Transfer," J. Chem. Phys. <u>56</u>, 900 (1972).

9. Akins, D.L., Fink, E.H., and Moore, C.B., "Rotation-Translation Energy Transfer Between Individual Quantum States of $HD(B^1\Sigma_u^+)$," J. Chem. Phys. <u>52</u>, 1604 (1970).

10. Fink, E.H., Wallach, D., and Moore, C.B., "Near-Resonant Electronic Energy Transfer from Argon to Hydrogen," J. Chem. Phys. <u>56</u>, 3608 (1972).

11. Carney, G.D. and Porter, R.N., "H_3^+: Ab Initio Calculation of the Vibration Spectrum," J. Chem. Phys. <u>65</u>, 3547 (1976).

12. Gentry, W.R., "Low Energy Pulsed Beam Sources," Chapter 3 in <u>Atomic and Molecular Beam Methods,</u> G. Scoles, Ed., to be published by Oxford University Press (   ).

13. Anderson, J.B. and Fenn, J.B., "Velocity Distributions in Molecular Beams from Nozzle Sources," Phys. Fluids <u>8</u>, 780 (1965).

REFERENCES CONTINUED

14. Fenn, J.B., "Collision Kinetics in Gas Dynamics," Appl. Atomic Collision Physics $\underline{5}$, 349 (1982).

15. Anderson, J.B., "Inviscid Freejet Flow with Low Specific Heat Ratios," AIAA J. $\underline{10}$, 112 (1972).

16. Boxall, M.J., Chapman, C.J., and Wayne, R.P., "Quenching of $Ar(^3P_1)$: Rate Constants for Deactivation and 'Escape Factors' for Trapped Radiation," J. Photochem. $\underline{4}$, 435 (1975).

17. Weise, W.L., Smith, M.W., and Miles, B.M., "Atomic Transition Probabilities, Volume II – Sodium Through Calcium, A Critical Data Complication," U.S., Department of Commerce, National Bureau of Standards, NSRDS-NBS 22, October 1969.

18. Hesser, J.E., "Absolute Transition Probabilities in Ultraviolet Molecular Spectra," J. Chem. Phys. $\underline{48}$, 2518 (1968).

19. Adams, T.E., Rockney, B.H., Morrison, J.S., and Grant, E.R., "Convenient Fast Pulsed Molecular Beam Valve," Rev. Sci. Inst. $\underline{52}$, 1469 (1981).

20. Grant, E.R., private communication.

21. Cobine, J.D., Gaseous Conductors, Theory and Engineering Applications, Dover Publications, Inc., New York (1958).

22. Spindler, R.J., Jr., "Franck-Condon Factors for Band Systems of Molecular Hydrogen. I. The $(B^1\Sigma_u - X^1\Sigma_g^+)$, $(I^1\Pi_g - B^1\Sigma_u^+)$, and $(d^3\Pi_u - a^3\Sigma_g^+)$ Systems," J. Quant. Spectrosc. Radiat. Transfer $\underline{9}$, 597 (1969).

23. Ajello, J.M., Srivastava, S.K., and Yung, Y.L., "Laboratory Studies of UV Emissions of H_2 by Electron Impact. The Werner-and-Lyman-Band Systems," Phys. Rev. A. $\underline{25}$, 2488 (1982).

24. Hessler, J.E., "Absolute Transition Probabilities in Ultraviolet Molecular Spectra," J. Chem. Phys., $\underline{48}$, 2518 (1968).

25. See, for example, Formation and Trapping of Free Radicals, edited by A.M. Bass and H.P. Broida (Academic, New York, 1960).

26. J. Berkowitz, W.A. Chupka, and G.B. Kistiakowsky, J. Chem. Phys. $\underline{25}$, 457 (1956).

27. J.T. Vanderslice, E.A. Mason, and E.R. Lippincott, J. Chem. Phys., $\underline{30}$, 129 (1959).

28. W.E. Meador, NASA Tech. Rep. TR-R-68 (1960).

29. R.F. Ferrante and W.C. Stwalley, J. Chem. Phys. $\underline{78}$, 3107 (1983).

REFERENCES CONTINUED

30. M. Capitelli, U.T. Lamanna, C. Guidotti, and G.P. Arrighini, J. Chem. Phys. $\underline{79}$, 5210 (1983).

31. H. Partridge, S.R. Langhoff, and C.W. Bauschlicher, Jr., J. Chem. Phys. $\underline{84}$, 6901 (1986).

32. R.S. Mulliken, J. Chem. Phys. $\underline{37}$, 809 (1962).

33. M. Krauss and D.B. Neumann, Mol. Phys. $\underline{32}$ 101 (1976).

34. P.E.M. Siegbahn, Int. J. Quantum Chem. $\underline{23}$, 1869 (1983).

35. P.K. Carroll, J. Chem. Phys. $\underline{37}$, 805 (1962).

36. Partridge, H., Langhoff, S.R., Bauschlicher, C.W., Jr., and Schwenke, D.W., "Theoretical Study of the $A'^5\Sigma_g{}^+$ and $C''^5\Pi_u$ States of N_2: Implications for the N_2 Afterglow," J. Chem. Phys. $\underline{88}$, 3174 (1988).

37. K.P. Huber and M. Vervloet, J. Chem. Phys. $\underline{89}$, 5957 (1988).

38. I. Nadler, D.W. Setser, and S. Rosenwaks, Chem. Phys. Lett. $\underline{72}$, 536 (1980).

39. I. Nadler, A. Rotem, and S. Rosenwaks, Chem. Phys. $\underline{69}$, 375 (1982).

40. L.G. Piper, J. Chem. Phys. $\underline{88}$, 231 (1988).

41. E.E. Eyler and F.M. Pipkin, J. Chem. Phys. $\underline{79}$, 3654 (1983).

42. King, D.S. and Schenck, P.K., "Optogalvanic Spectroscopy," Laser Focus, 50 (March 1978).

43. Webster, C.R. and Retter, C.T., "Laser Optogalvanic Spectroscopy of Molecules," Laser Focus, 41 (February 1983).

44. Feldmann, D., "Opto-Galvanic Spectroscopy of Some Molecules in Discharges: NH_2, NO_2, H_2 and N_2," Optics Comm. $\underline{29}$, 67 (1979).

45. Sibener, S.J., Buss, R.J., Ng, C.Y., and Lee. Y.T., "Development of a Supersonic $O(^3P_j)$, $O(^1D_2)$ Atomic Oxygen Nozzle Beam Source," Rev. Sci. Instrum. $\underline{51}$, 167 (1980).

46. A. Fontijn, C.B. Meyer, and H.L. Schiff, J. Chem. Phys. $\underline{40}$, 64 (1964).

47. D.W. Setser, D.H. Stedman, and J.A. Coxon, J. Chem. Phys. $\underline{53}$, 1004 (1970).

48. D.H. Stedman and D.W. Setser, Chem. Phys. Lett. $\underline{2}$, 542 (1968).

REFERENCES CONTINUED

49. E.E. Ferguson, F.C. Fehsenfeld, and A.L. Schmeltkopf, Adv. At. Mol. Phys. V, 1 (1970).

50. W.J. Moore, Physical Chemistry, Prentice-Hall, Inc. Englewood Cliffs, NJ, 162 (1972).

51. H. Geisen, D. Neuschäfer, and Ch. Ottinger, Z. Phys. D - Atoms, Molecules and Clusters 4, 263 (1987).

52. A. Lofthus and P.H. Krupenie, J. Phys. Chem. Ref. Data 6, 113 (1977).

53. L.G. Piper, J. Chem. Phys. 88, 6911 (1988).

54. Zare, R.N., "Angular Momentum," in Understanding Spatial Aspects in Chemistry and Physics, Eds. John Wiley & Sons, Wiley-Interscience Publication, 1988.

55. Windsor, M.W., "Trapped Radicals in Propulsion," in Formation and Trapping of Free Radicals (Academic Press, New York, A.M. Bass and H.P. Brodia, eds.) 1960, p. 387-409.

56. Bass, A.M. and Broida, H.P., Stabilization of Free Radicals at Low Temperatures, National Bureau of Standard, Monograph 12, USGPO, Washington, DC, 1960.

57. Broida, H.P. and Pellam, J.R., "Phosphorescence of Atoms and Molecules of Solid Nitrogen at 4.2 K," Phys. Rev. 95, 845 (1954).

58. Bass, A.M. and Broida, H.P., "Spectra Emitted from Solid Nitrogen Condensed at 4.2 K from a Gas Discharge," Phys. Rev. 101, 1740 (1956).

59. Peyron, M. and Broida, H.P., "Spectra Emitted from Solid Nitrogen Condensed at Very Low Temperatures from a Gas Discharge," J. Chem. Phys. 30, 139 (1959).

60. Broida, H.P. and Peyron, M., "Emission Spectra of N_2, O_2, and NO Molecules Trapped in Solid Matrices," J. Chem. Phys. 32, 1068 (1960).

61. Brocklehurst, B. and Pimentel, G.C., "Thermoluminescence of Solid Nitrogen After Electron Bombardment at 4.2 K," J. Chem. Phys. 36, 2040 (1962).

62. Dressler, K., Oehler, O., and Smith, D.A., "Measurement of Slow Vibrational Relaxation and Fast Vibrational Energy Transfer in Solid N_2," Phys. Rev. Lett. 34, 22 (1975).

63. Oehler, O., Smith D.A., and Dressler, K., "Luminescence Spectra of Solid Nitrogen Excited by Electron Impact," J. Chem. Phys. 66, 2097 (1977); Dressler, K., in Molecular Spectroscopy of Dense Phases, edited by M. Grossman et al. (elsevier, Amsterdam, 1976), p. 355.

REFERENCES CONTINUED

64. Kunsch, P.L. and Dressler, K., "Calculation of Dynamically Induced Electronic Transitions of Matrix-Isolated Atomic Nitrogen," J. Chem. Phys. 68(6), 2550 (1978).

65. Vegard, L., "The Luminescence from Solidified Gases down to the Temperature of Liquid Hydrogen and its Application to Cosmic Phenomena," Leiden Comm. No. 175 (1924).

66. Vidaud, P.F., Wayne, R.P., Yaron, M., and von Engel, A., "Collisional Quenching of $N_2(A^3\Sigma_u^+; v=0,1)$ by N-Atoms, Ground State N_2 and a Pyrex Surface," J. Chem Soc. 72, 1185 (1976).

67. Meyer, J.A., Setser, D.W., and Stedman, D.H., "Energy Transfer Reactions of $N_2(A^3\Sigma_u^+)$. II. Quenching and Emission by Oxygen and Nitrogen Atoms," J. Phys. Chem. 74, 2238 (1970).

68. Young, R.A. and St. John, G.A., "Experiments on $N_2(A^3\Sigma_u^+)$. I. Reaction with N^*," J. Chem. Phys. 48, 895 (1968).

69. Wiese, W.L., Smith, M.W., and Glennon, B.M., "Atomic Transition Probabilities, Volume I Hydrogen Through Neon," National Standard Reference Data Series National Bureau of Standards 4, (Category 3) Issued May 29, 1966.

70. Tinti, D.S. and Robinson, G.W., "Spectroscopic Evidence for Slow Vibrational and Electronic Relaxation in Solids. The Vegard-Kaplan and Second Positive Systems of N_2 in Solid Rare Gases," J. Chem. Phys. 49(7), 3229 (1968).

71. Happer, W., Bonin, K.D., and Walker, T.G., "The Stability of Spin-Polarized Nitrogen Crystals," Chem. Phys. Lett. 135(4,5) 451 (1987).